



Inferring methane emissions from African livestock by fusing drone, tower, and satellite data

Alouette van Hove¹, Kristoffer Aalstad¹, Vibeke Lind², Claudia Arndt³, Vincent Odongo³, Rodolfo Ceriani^{4,5}, Francesco Fava⁵, John Hulth¹, and Norbert Pirk¹

¹Department of Geosciences, University of Oslo (UiO), Oslo, Norway

²Norwegian Institute of Bioeconomy Research (NIBIO), Tjøtta, Norway

³Mazingira Centre, International Livestock Research Institute (ILRI), Nairobi, Kenya

⁴Department of Agricultural and Environmental Sciences, University of Milan (UNIMI), Milan, Italy

⁵Department of Environmental Science and Policy, University of Milan (UNIMI), Milan, Italy

Correspondence: Alouette van Hove (a.van.hove@geo.uio.no)

Abstract.

Considerable uncertainties and unknowns remain in the regional mapping of methane sources, especially in the extensive agricultural areas of Africa. To address this issue, we developed an observing system that estimates methane emission rates by assimilating drone and flux tower observations into an atmospheric dispersion model. In this study, we apply this approach to

5 verify and quantify potential methane sources identified through radiance anomalies observed in hyperspectral satellite data. We compare different methods to estimate emissions from various ruminant livestock species in sub-Saharan Africa, including diverse herds of cattle, goats, and sheep, as well as camels, for which methane emission estimates are particularly sparse. Our estimates, derived from Bayesian inference, align with Tier 2 emission values of the Intergovernmental Panel on Climate Change. We moreover observe the hypothesized increase in methane emissions following feeding. Our findings suggest that

10 the Bayesian inference method is more robust under non-stationary wind conditions compared to a mass balance approach using drone observations. Furthermore, the Bayesian inference method performs better in quantifying emissions from weaker sources, estimating methane emission rates as low as 100 g h^{-1} . We find a $\pm 50\%$ uncertainty in emission rate estimates for these weaker sources, such as sheep and goat herds, which reduces to $\pm 12\%$ for stronger sources, like cattle herds emitting $1,000 - 1,500 \text{ g h}^{-1}$. These promising results demonstrate the potential and efficacy of the Bayesian inference method for

15 source term estimation. Future applications of drone-based Bayesian inference could extend to estimating methane emissions in Africa and other regions from various sources with complex spatiotemporal emission patterns, such as wetlands, landfills, and wastewater disposal sites. The Bayesian observing system could thereby contribute to the validation and improvement of climate models and emission inventories.

1 Introduction

20 While methane (CH_4) emissions from so-called super-emitters ($> 100 \text{ kg h}^{-1}$) can be quantified using satellite data, the current spatial resolution and spectral resolution, as well as the precision of satellite observations, are not sufficient to effectively



quantify weaker sources, such as livestock herds (Sherwin et al., 2023). To address this limitation and complement the regional mapping of CH₄ sources of various strengths, we developed an observing system that uses a Bayesian inference approach to assimilate drone and flux tower observations in an atmospheric dispersion model to estimate CH₄ emission rates. We assess the efficacy of the Bayesian inference method in quantifying CH₄ emissions from nine different ruminant herds in sub-Saharan Africa - an important, yet poorly understood, source in the global CH₄ emission inventory. By comparing our results to those obtained using a mass balance method with drone observations and to emission values of the Intergovernmental Panel on Climate Change (IPCC) (Gavrilova et al., 2019), we demonstrate the effectiveness and robustness of our approach.

Global mean atmospheric CH₄ concentrations surpassed 1.90 ppm in 2022, marking a 16 % increase since 1985 (Lan et al., 2024). Livestock production is a major contributor to global anthropogenic CH₄ emissions, accounting for approximately one-third of the total emissions (Saunois et al., 2020). Within this sector, enteric fermentation in ruminants - such as cattle, sheep, goats, and camels - is the predominant source, generating approximately 80 % of these emissions, while the remaining 20 % originates from manure (Amon et al., 2001). During the digestive process, CH₄ is produced by rumen fermentation, with about 90 – 95 % released through burping and 5 – 10 % as intestinal gas (Broucek, 2014). Because CH₄ has a high global warming potential and a relatively short atmospheric lifetime, reducing its emissions can have quick benefits in mitigating climate change (Szopa et al., 2021). Therefore, accurate measurements and understanding of CH₄ emissions from ruminants are important for developing effective mitigation strategies and evaluating their efficacy.

The IPCC provides internationally recognized standardized methodologies for estimating CH₄ emissions from ruminants (Gavrilova et al., 2019). Tier 1 methods use generalized default values for emission factors, which are often continent or region specific. In contrast, Tier 2 values incorporate more detailed herd-specific or animal-specific data. These data account for local variations in livestock breeds, manure management practices, feed quality, and environmental conditions. Recent studies from sub-Saharan Africa have demonstrated substantial differences between emission estimates from these two tiers (Goopy et al., 2018; Ndung'u et al., 2019; Gurmu et al., 2024), highlighting the need for precise, locally relevant data. However, there is a scarcity of studies focusing on CH₄ emission rates from ruminants in this region. Many studies use energy balance estimates based on factors such as animal weight, feed, and activity level, with few studies actually measuring CH₄ concentrations (as done by e.g., Korir et al., 2022a; Goopy et al., 2020; Mwangi et al., 2023; Wolz et al., 2022). We aim to contribute to help bridge this knowledge gap.

Specifically, research on CH₄ emissions from camels is sparse. Although a few studies have estimated emissions using direct CH₄ measurements from smaller camelids such as alpacas and llamas (e.g., Pinares-Patiño et al., 2003; Nielsen et al., 2014), research on larger camelids, like dromedaries and Bactrian camels, remains limited. This lack of data is likely due to the respiration chambers used for measuring gas exchange being too small to fit these larger animals. Nonetheless, Dittmann et al. (2014) conducted respiration chamber measurements with Bactrian camels. Our study represents one of the first efforts to estimate CH₄ emissions from camels, specifically dromedaries, thereby contributing to the development of knowledge in a relatively unstudied field.

Gas exchange methods such as respiration chambers and headboxes are typically used to quantify CH₄ emissions from individual animals. For estimating emissions from ruminant herds or entire farm facilities, several indirect techniques have been



applied. Tracer-ratio experiments (Vechi et al., 2022; Daube et al., 2019; Arndt et al., 2018) involve releasing a known quantity of a tracer gas and comparing its dispersion to that of CH₄. The mass balance approach (Vinković et al., 2022; Arndt et al., 2018; Wratt et al., 2001) calculates emissions based on the difference between incoming and outgoing CH₄ flux estimates in a defined volume. Other studies (Wolz et al., 2022; Bai et al., 2021; Arndt et al., 2018) use open-path Fourier transform infrared or laser spectrometry to obtain horizontal path-integrated CH₄ concentrations upwind and downwind from the source. These concentration data are combined with a Lagrangian particle dispersion model to estimate emission rates. Inverse modeling techniques (Andersen et al., 2021) infer emission rates by fitting an atmospheric dispersion model to measured atmospheric data, possibly incorporating prior knowledge.

On much larger spatial scales, satellite observations are frequently used to detect and quantify CH₄ emissions from super-emitters, such as leaks from oil and gas production and large landfills (e.g., Pandey et al., 2019; Dogniaux et al., 2024). However, the emission rates of livestock herds are much smaller, and therefore more challenging to identify as potential CH₄ sources from satellite data. To accurately map the emission plumes from these weaker sources, measurement platforms with a higher spatial resolution are needed.

The advent of drone technology as a versatile platform for carrying measurement equipment has enabled high-resolution spatiotemporal observations of atmospheric gases and thermodynamic variables (Villa et al., 2016; Burgués and Marco, 2020). This innovation allows for data collection over a larger spatial region than fixed flux towers or monitoring stations and offers higher spatial resolution compared to satellite-based measurements. Moreover, drones facilitate measurements in locations that are otherwise inaccessible to crewed aircrafts due to safety reasons, such as areas close to the CH₄ source and near the ground.

In our study, we utilize drones to sample and map CH₄ emission plumes from African ruminant herds, leveraging this data to estimate their CH₄ production. Notably, this research is, as far as we know, a pioneering effort to employ drones for CH₄ emission quantification from ruminants in sub-Saharan Africa. We apply two distinct methods: a traditional mass balance method and an innovative Bayesian inference approach that uses a sequential Monte Carlo method to invert an atmospheric diffusion model. To complement this analysis, we assess the capability of hyperspectral satellite data to pinpoint the location of CH₄ sources, specifically ruminant herds, by identifying spectral anomalies at the landscape level.

While Bayesian inference has previously been applied with drone observations in homogeneous environments with artificial gas sources (Hutchinson et al., 2019, 2020; Park et al., 2021), to the best of our knowledge, this research marks the first application of the method for quantifying ruminant emissions in real-world conditions using drone observations. The Bayesian framework addresses uncertainties in atmospheric observations, potentially enhancing the precision and reliability of emission estimates. Furthermore, it allows for the integration of observations from multiple platforms, including drones and flux towers. We explore which sensor observations - specifically CH₄ concentration measurements and wind measurements, either from the drone or the flux tower - are most effective for applying the Bayesian inference approach.

We aim to achieve the following objectives: (1) To investigate whether spectral indices related to CH₄ emissions from hyperspectral satellite data can aid in detecting the locations of CH₄ sources, specifically ruminant herds. (2) To evaluate the efficacy of the Bayesian inference method utilizing drone-based observations for estimating CH₄ emission rates. (3) To determine emission rates for free-grazing cattle, sheep, goats, and camels in a sub-Saharan African country using drone-based



observations. (4) To compare the results obtained from the Bayesian inference method with estimates from a mass balance method and IPCC Tier 2 values, to evaluate different methods for estimating CH₄ emissions from ruminants in sub-Saharan Africa and to contribute to the improvement of national greenhouse gas inventories.

95 2 Materials and methods

This study was conducted at the Kapiti Research Station in Kenya, approximately 60 km south-east from Nairobi. The station is managed by the International Livestock Research Institute (ILRI). Covering over 13,000 hectares, the station houses various ruminants, including cattle, sheep, goats, and camels, with a primary focus on studying livestock productivity. Livestock management at Kapiti follows typical pastoral systems, where herders allow the animals to graze freely during the day and keep
100 them in enclosures, known in Kenya as bomas, during the night.

This section outlines the different methodologies used in this study to detect and estimate CH₄ sources. We apply four approaches: (1) CH₄ source location detection through hyperspectral satellite observations, and three methods for source term estimation: (2) CH₄ source term estimation through drone observations using a particle-based Bayesian inference method, (3) CH₄ source term estimation through drone observations using a mass balance approach, and (4) calculation of IPCC Tier 2
105 emission values.

2.1 Satellite observations for source detection

In an exploratory effort, we investigate the potential for detecting livestock herds as CH₄ sources using satellite hyperspectral imagery. On 6 March 2024, the PRecursores IperSpettrale della Missione Applicativa (PRISMA) satellite (Loizzo et al., 2018) was commissioned to capture a hyperspectral image of Kapiti, while three cattle herds were present at different sites. The
110 PRISMA satellite has two hyperspectral sensors that cover a spectral range from 400 nm to 2500 nm. Methane exhibits strong absorption features in the Shortwave Infrared (SWIR) region between 2150 nm and 2500 nm, with particularly strong absorption around 2300 nm (Moorhead, 1932; Brown et al., 2003; Roger et al., 2024a). Consequently, the Simple Ratio (SR) index of the wavelengths at 2300 nm and 2100 nm (SR_{2300/2100}) is commonly used to detect spatial variations in CH₄ absorption (Xiao et al., 2020; Scafutto et al., 2021; Roger et al., 2024b; Pei et al., 2023). A lower SR indicates lower relative radiance
115 at 2300 nm and thus greater absorption, suggesting higher atmospheric CH₄ concentrations. However, it is important to note that spatial variations in other factors, such as vegetation water content, leaf structure, and soil moisture, can also influence the SR index.

We process the hyperspectral data of the PRISMA satellite in the infrared region to detect spatial variations in the CH₄ absorption feature. Starting from Level-1 top-of-atmosphere radiance narrowbands (Giardino et al., 2020), infrared information
120 is integrated into single data cubes using the PRISMAREAD package in the R environment (Busetto and Ranghetti, 2020). This produces hyperspectral data cubes consisting of 173 bands, spanning infrared wavelengths from 920 nm to 2505 nm. Finally, we calculate the SR index for each data cube using the SWIR wavelengths at 2300 nm and 2100 nm.



2.2 Drone-based source term estimation

This section provides details of the drone field campaign, conducted between 29 February and 7 March 2024 at Kapiti. It
125 outlines both the Bayesian inference method and the mass balance approach used to estimate CH₄ emission rates from drone
observations.

We use a drone equipped with a gas sensor to obtain CH₄ concentration observations of the emission plumes of nine different
ruminant herds: cattle (cows, heifers, steers, and slick herd), sheep (lactating ewes), goats (dry does, pregnant does, weaner
kids), and camels. The cows, heifers, and steers are Boran cattle, while the slick herd is a crossbreed between Holstein-Friesian
130 and Boran heifers. The sheep flock consists of Red Masaai and Dorper, and the goat herds comprise Small East African and
Galla varieties. The camels are dromedaries. The lactating ewes had lambs, and the pregnant does had kids with them. However,
since the rumen fermentation systems of milk-fed lambs and kids are not yet fully developed (Baldwin et al., 2004), we assume
their CH₄ emissions to be negligible and treat these herds as if the lambs and kids were not present. The herd sizes are included
in Table B1.

135 During the drone flights, the respective herds were confined within a boma at coordinates -1.61365°N , 37.13234°E . The
animals exhibited no signs of distress and appeared at ease throughout the drone operations. Figure 1 shows the heifers inside
the boma during a drone flight that coincided with the satellite overpass, as well as a herd of camels observing a passing drone.

Typically, four flights were conducted for each ruminant herd. In the morning, before grazing, two flights were performed:
one flight for each emission estimation method, namely the Bayesian inference approach and a mass balance approach. The
140 same set of flights was repeated in the afternoon after the animals had grazed. Feed intake is known to increase enteric CH₄
emissions in ruminants, with peak emissions occurring shortly after feeding (Amon et al., 2001; Hegarty, 2013). Since the
animals had no access to feed during the night, lower emissions are expected in the morning compared to the afternoon,
following grazing. We investigate whether there is a noticeable increase in CH₄ emissions between the morning and afternoon
flights, using consistent observations of such increases as indicators of the method's reliability and accuracy.

145 During control drone flights, conducted without animals present in the boma or the immediate surroundings, no increase
in CH₄ levels was observed throughout the field campaign. Based on this observation, we assume that CH₄ production from
manure is negligible in our study and attribute the elevated CH₄ concentrations above the background level solely to enteric
fermentation.

2.2.1 Observing system

150 Our observing system consists of a DJI M300 RTK drone equipped with an AERIS MIRA Strato LDS CH₄ gas sensor, as well
as a stationary flux tower with an eddy covariance system (Burba, 2013). The tower is located at coordinates -1.61419°N ,
 37.13313°E , approximately 100m south-south-east from the center of the boma, as shown in Fig. 2.

The drone's position was recorded using Real-Time Kinematic (RTK) positioning. A Digital Elevation Model (DEM) of the
area was obtained using DJI L1 Lidar, processed in DJI Terra. The altitude data of the RTK system was corrected using the



Figure 1. (a) A drone flight capturing methane concentration observations of a heifer herd coinciding with the satellite overpass on 6 March 2024. (b) Camels inside the boma during a drone flight on 4 March 2024. Of all animals, the camels were the most curious about the drone.

155 DEM at the drone's home location. Additionally, the DEM was used to determine the drone's flight height above the ground surface.

The AERIS MIRA Strato LDS gas analyzer detects CH_4 using mid-infrared laser spectroscopy, which measures the absorption of infrared radiation by CH_4 molecules. The reported mixing ratio X [ppm; parts per million per volume] at the point measurement is the fraction of CH_4 molecules per million molecules of air. The sensor has a sensitivity of 1 ppb and a sampling
160 rate of 1 Hz. The mixing ratio X is converted to mass concentration c [g m^{-3}] using the ideal gas law, where the ambient air temperature and pressure are obtained from the flux tower.

Wind data were collected using two sensor platforms: a fixed flux tower and the drone. Wind data was captured by the 3D sonic anemometer mounted on the tower at a height of 5 m above the ground. The wind speed and wind direction data were resampled from 10 Hz to 1 Hz to match the timestamps of the CH_4 sensor. The data from the eddy-covariance system was processed at half-hour intervals using EddyPro (Li-Cor) to determine the Obukhov length L [m] and friction velocity u_* [m s^{-1}]. Using Monin Obukhov Similarity Theory (MOST; see Stull, 1989), we estimate the vertical profile of the mean
165 wind speed $V(z)$ [m s^{-1}] and mean eddy diffusivity $K(z)$ [$\text{m}^2 \text{s}^{-1}$], where z is the distance above the ground. Appendix A includes details on the application of MOST.

The drone quantifies wind speed using its onboard sensors to measure resistance during stable hover or flight. This data,
170 combined with the drone's GPS and inertial measurement unit (IMU), allows for estimations of wind speed and direction by analyzing the accelerations and attitude adjustments needed to counteract the wind's force (Abichandani et al., 2020). Wind data from the drone were obtained from the flight logs using the Flight Reader software.

Given concerns that the additional bulk and weight of the CH_4 sensor might affect readings, we performed a correction for wind speed. During the field campaign, the drone hovered for a total of 90 minutes a couple of meters downwind from the
175 sonic anemometer under various wind speeds and orientations relative to the wind direction. Wind speed data from the drone were corrected through linear regression against the sonic anemometer data (Fig. S1 in Supplementary Material). The wind

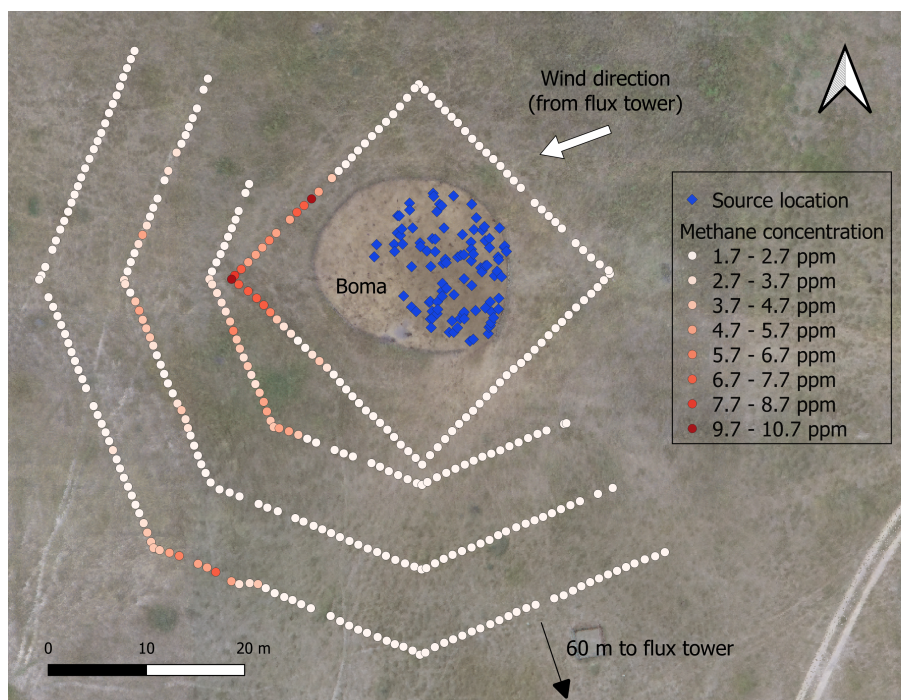


Figure 2. Top-down view of the drone flight paths capturing CH₄ concentration observations in the afternoon of 6 March 2024. Shown are CH₄ concentration measurements obtained at a height of 2.7 m during the mass balance flight around the boma, and at heights of 3.5 m, 3.0 m, 2.5 m during the half-octagon flight for the Bayesian inference method. The blue markers indicate the source location in the atmospheric dispersion model, representing the heifer herd. The wind direction arrow shows the mean wind direction observed by the flux tower.

direction is reported by the drone in eight compass directions. The wind direction data did not qualitatively match well with the sonic anemometer data and were therefore not used in our study (Fig. S2 in Supplementary Material).

2.2.2 Bayesian inference method

180 The first drone-based method for quantifying CH₄ emission rates utilizes an inverse modeling approach, which assimilates atmospheric measurements into an atmospheric transport model to infer emission rates. Two principal approaches are commonly employed in model inversion: (1) Several studies (Andersen et al., 2021; Shah et al., 2019, 2020) minimize a cost function to find the best fit between a Gaussian plume model (Sutton, 1947) and observed CH₄ concentrations. (2) In the field of robotics, various studies employ a Bayesian inference approach to model inversion in order to estimate source emission rates and source
185 locations, among other unknown variables, at local scales (Hutchinson et al., 2017; Francis et al., 2022). Unlike optimization, the Bayesian approach is particularly well suited to solving ill-posed inverse problems involving the assimilation of noisy observations that are ubiquitous in geophysics (Sanz-Alonso, 2023). Beyond robotics, Bayesian frameworks are also utilized



in estimating carbon emissions on regional or global scales from satellite observations (Cusworth et al., 2021; Western et al., 2021) and international ground-based atmospheric observation networks (Evangelidou et al., 2018; Thompson et al., 2022).

190 We adopt a Bayesian approach, providing a probabilistic interpretation of the model parameters and including uncertainty quantification of the parameter estimates. Previous research has demonstrated the efficacy of Bayesian inference with synthetic drone observations for source localization and estimation (Loisy and Eloy, 2022; van Hove et al., 2024b). However, its applications in real-world environments at a local scale remain relatively limited. Hutchinson et al. (2019) and Park et al. (2021) successfully deployed Bayesian inference methods in outdoor experiments with flat, homogeneous terrain and time-invariant
195 controlled-release sources, while Hutchinson et al. (2020) explored emissions from a car crash and oil rig at a test site. In real-world conditions, Pirk et al. (2022) assimilated drone observations within a Bayesian framework to infer turbulent fluxes of sensible and latent heat of a wetland and a palsa mire in Norway.

We use the advection-diffusion model formulated by Vergassola et al. (2007) to simulate CH₄ transport under turbulent atmospheric conditions. This model has been shown by Hutchinson et al. (2019) to more accurately represent small-scale
200 plume behavior compared to the Gaussian plume model. The mean stationary concentration c [g m⁻³] at measurement location $\mathbf{x} = [x, y, z]$ is given by

$$c(\mathbf{x}, \mathbf{x}_s) = \frac{Q/\alpha}{4\pi D|\mathbf{x} - \mathbf{x}_s|} \exp\left(\frac{-(x - x_s)V \sin(\phi)}{2D}\right) \exp\left(\frac{-(y - y_s)V \cos(\phi)}{2D}\right) \exp\left(\frac{-|\mathbf{x} - \mathbf{x}_s|}{\lambda}\right) + c_0, \quad (1)$$

where $\mathbf{x}_s = [x_s, y_s, z_s]$ represents the source location, Q [g h⁻¹] denotes the CH₄ emission rate, $\alpha = 3600$ s h⁻¹ is the time conversion factor from hours to seconds, V [m s⁻¹] represents the mean wind speed, ϕ [°] is the mean wind direction, D [m² s⁻¹]
205 denotes the effective diffusivity, λ [m] is a characteristic length scale, and c_0 [g m⁻³] is the mean stationary background concentration. We make a distinction between the emission rate of the entire herd, denoted by Q [g h⁻¹], and the emission rate per individual animal, denoted by q [g head⁻¹ h⁻¹].

The instantaneous wind fluctuates in amplitude and direction due to effective diffusivity D , which is the sum of turbulent diffusivity and the typically much smaller molecular diffusivity. Unlike the Gaussian plume model, which uses dispersion
210 parameters σ_y and σ_z , typically determined by the stability classification schemes of Pasquill (1961), effective diffusivity D is directly incorporated in the model. Consequently, by making the assumption $D \approx K$, observational estimates of D can be obtained via MOST, as detailed in Appendix A.

The length scale λ in Eq. (1) is defined as

$$\lambda = \sqrt{\frac{D\tau}{1 + \frac{V^2\tau}{4D}}}, \quad (2)$$

215 where D denotes the effective diffusivity, V is the mean wind speed, and τ is the finite lifetime of CH₄ in the atmosphere, approximately 9.1 years (Prather et al., 2012).

To conserve CH₄ mass in Eq. (1), the ground is modeled as a perfect reflector of the plume, as is typically done in Gaussian plume modeling (Hanna et al., 1982). This is achieved by including a mirror image source below the ground surface: $\mathbf{x}_{s, \text{mirror}} = -\mathbf{x}_s$. Consequently, the total concentration field becomes the sum of the original and mirrored sources: $c(\mathbf{x}, \mathbf{x}_s) \leftarrow c(\mathbf{x}, \mathbf{x}_s) +$
220 $c(\mathbf{x}, \mathbf{x}_{s, \text{mirror}})$.



In our study, emission rate Q , mean wind speed V , mean wind direction ϕ , and effective diffusivity D in Eq. (1) are treated as unknown parameters to be inferred through model inversion. The parameters that are assumed to be known include the source location \mathbf{x}_s , drone locations \mathbf{x} , and background concentration c_0 , which have been determined as follows. On the small spatial scale of our study, approximating the herd of animals as a single point source would be an over-simplification. Instead, we model the herd as a set of m sources, resulting in a total concentration field that is the sum of the individual concentrations from these sources: $c(\mathbf{x}, \mathbf{x}_s) \leftarrow \sum_i^m c(\mathbf{x}, \mathbf{x}_{s,i})$. This source superposition is commonly used in Gaussian plume modeling (e.g. Calder (1977)). Using aerial photographs taken during the drone flights, we randomly select $m = 100$ source locations within the outline of the herd, which together are responsible for emission rate Q . For example, the 100 blue markers within the boma shown in Fig. 2 represent the source location of a heifer herd. After inferring emission rate Q , we normalize by the actual number of animals in the herd to obtain the emission rate per individual animal q . The source height z_s is estimated by averaging the mouth height of 10 animals from each herd, based on direct measurements. The mean background concentration for each drone flight is empirically determined by calculating the median of the CH_4 concentration observations that fall below the threshold of 1.8 ppm.

The drone flew nine legs in a half-octagon pattern downwind of the herd at three different distances: approximately 40 m, 30 m, and 20 m from the center of the boma. The corresponding heights for the outer legs were approximately 3.5 m, 5.5 m, and 9.0 m; for the middle legs, 3.0 m, 4.5 m, and 7.0 m; and for the inner legs, 2.5 m, 3.5 m, and 5.0 m above ground level. To minimize the effects of rotor downwash (visualized with colored smoke in Crazzolaro et al. (2019)) and downwind disturbances to the plume (visualized with colored smoke in Hutchinson et al. (2019)), the flights were performed from the outer to the inner legs, starting at the lowermost altitude and ascending to higher altitudes. Figure 2 offers a top-down view of the boma and illustrates the measured CH_4 concentrations along the lowest three legs of the half-octagon flight plan during the drone flight with a herd of heifers on the same day as the satellite overpass.

In our study, we explore the use of three different observing systems for model inversion:

- (a) **CH_4 concentration data:** We assimilate only instantaneous drone-based CH_4 concentration data as observations for c .
- (b) **CH_4 concentration data with drone-derived wind speed:** We assimilate the same concentration data (observation case (a)) along with mean wind speed observations V_{obs} derived from drone data. The average wind speed is calculated over the estimated plume depth of 8 m. Specifically, wind speed data from the drone flight is averaged over 1 m vertical intervals up to 8 m, and the overall average is then obtained over these interval-specific averages.
- (c) **CH_4 concentration data with flux tower data:** We assimilate CH_4 concentration data (observation case (a)) in combination with observations for mean wind speed V_{obs} , mean wind direction ϕ_{obs} , and effective diffusivity D_{obs} derived from the flux tower data. Hereby, we make the approximation that $D \approx K$, and assume that the vertical and horizontal diffusivity are equal, as is done in Eq. (1). We obtain mean wind speed and diffusivity values by averaging their respective profiles - Eq. (A1) and Eq. (A3) - over the estimated vertical plume extent of 8 m.

We employ a probabilistic approach to model inversion, applying Bayesian inference recursively to mini-batches of observational data to make the problem more computationally tractable (Chopin, 2002). At each new iteration step $n + 1$, the



255 dynamic prior probability distributions of the unknown parameters $p(\boldsymbol{\theta}|\mathbf{d}_{0:n})$ are updated to the posterior probability distributions $p(\boldsymbol{\theta}|\mathbf{d}_{0:n+1})$ given a new mini-batch of observations \mathbf{d}_{n+1} via Bayes' rule

$$p(\boldsymbol{\theta}|\mathbf{d}_{0:n+1}) = \frac{p(\mathbf{d}_{n+1}|\boldsymbol{\theta})p(\boldsymbol{\theta}|\mathbf{d}_{0:n})}{p(\mathbf{d}_{n+1}|\mathbf{d}_{0:n})}, \quad (3)$$

where the conditional model evidence (or marginal likelihood) acts as a normalizing constant

$$p(\mathbf{d}_{n+1}|\mathbf{d}_{0:n}) = \int p(\mathbf{d}_{n+1}|\boldsymbol{\theta})p(\boldsymbol{\theta}|\mathbf{d}_{0:n})d\boldsymbol{\theta}. \quad (4)$$

260 At each new iteration $n+1$, the dynamic prior distributions $p(\boldsymbol{\theta}|\mathbf{d}_{0:n})$ are simply the corresponding dynamic posteriors from the previous iteration n . The use of such sequential Bayesian updating makes the inference problem more computationally tractable and is a key property of the sequential Monte Carlo methods that we employ in practice (Chopin and Papaspiliopoulos, 2020). Note the slight abuse of notation where \mathbf{d}_0 is implicitly empty, and thus $p(\boldsymbol{\theta}|\mathbf{d}_0)$ - rather than the usual $p(\boldsymbol{\theta})$ - denotes the initial prior at $n = 0$ for notational convenience.

265 The likelihood term $p(\mathbf{d}_{n+1}|\boldsymbol{\theta})$ in Eq. (3) links the observations to the forward model, effectively serving as a measure of discrepancy between the observed data and the model predictions. The observational model relating observations \mathbf{d} to the forward model prediction is given by

$$\mathbf{d} = \mathcal{F}(\boldsymbol{\theta}) + \boldsymbol{\epsilon}, \quad (5)$$

where $\boldsymbol{\epsilon}$ represents the discrepancy (or residual) term, explicitly capturing the various sources of error in the measured data (and implicitly also errors in the model). For the CH_4 concentration observations c_{obs} , the forward model \mathcal{F} is defined by Eq. (1). In the case of the wind and diffusivity observations, \mathcal{F} is a more direct noisy mapping; for example, the observed mean wind speed V_{obs} is modeled as $V_{\text{obs}} = V + \epsilon_V$.

As Rao (2005) identifies, discrepancies in atmospheric dispersion modeling can arise due to: (a) noise in the sensor measurements, (b) errors in the model input data, (c) the fact that atmospheric dispersion models are imperfect, and (d) inherent randomness in unresolved turbulent dispersion processes. Given the limited knowledge of these errors, the Gaussian distribution is the most conservative choice for the likelihood function according to the maximum entropy principle (Jaynes, 2003). Thus, we define the likelihood function as a Gaussian of the form $p(\mathbf{d}_{n+1}|\boldsymbol{\theta}) = \mathcal{N}(\mathbf{d}_{n+1}|\mathcal{F}(\boldsymbol{\theta}), \mathbf{R})$ where the mean vector $\mathcal{F}(\boldsymbol{\theta})$ contains the model predictions and \mathbf{R} is a diagonal observation error covariance matrix with observation error variances σ^2 along the diagonal. These observation error variances correspond to the respective observation error standard deviations empirically estimated as $\sigma_c = 1 \text{ ppm}$, $\sigma_V = 0.30 \text{ ms}^{-1}$, $\sigma_\phi = 10^\circ$, and $\sigma_D = 0.15 \text{ m}^2 \text{ s}^{-1}$ for concentration c , mean wind speed V , wind direction ϕ , and effective diffusivity D , respectively.

We recognize a discrepancy between the timescales of our concentration observations and the statistical assumptions of our dispersion model presented by Eq. (1): while the observations are instantaneous samples of a turbulent boundary layer, our model represents a time-averaged plume. This discrepancy or representation error (Van Leeuwen, 2015) is expected to be the largest source of uncertainty in our Bayesian inference approach. Additional sources of uncertainty include the assumption of a fixed vertical plume extent, ignoring uncertainties inherent in the (assumed) known variables such as the background



concentration, among other factors. To account for these approximations and minimize the impact of potential errors, we incorporate a high level of uncertainty into the likelihood term by inflating the observation error covariance \mathbf{R} to match the aforementioned observation error standard deviations.

290 The initial prior distributions $p(\boldsymbol{\theta}|\mathbf{d}_0)$ are chosen to be flat non-informative priors in the form of uniform distributions across defined ranges to match reasonable prior expectations (Banner et al., 2020): $q \sim \mathcal{U}(0.36, 36.00) \text{ g head}^{-1} \text{ h}^{-1}$, $V \sim \mathcal{U}(0, 6) \text{ m s}^{-1}$, $\phi \sim \mathcal{U}(-45, 135)^\circ$, corresponding to the wind compass half of the prevailing wind direction, and $D \sim \mathcal{U}(0.3, 3.0) \text{ m}^2 \text{ s}^{-1}$. We implement the Bayesian inference framework in Python (available from van Hove et al. (2024a)) by a Sequential Monte Carlo (SMC) framework (Chopin and Papaspiliopoulos, 2020; Särkkä and Svensson, 2023) that generalizes the classic boot-
295 strap particle filter (Gordon et al., 1993). This method approximates the probability distributions with a set of weighted ensemble members, referred to as particles. In each iteration, the weights of these particles are updated based explicitly on their likelihood, representing their fit to the observed data, and implicitly on the dynamic prior. To address the particle degeneracy problem, where only a few particles retain significant weights, we apply the resample-move algorithm (Gilks and Berzuini, 2001; Doucet and Johansen, 2009). This algorithm enhances the particle diversity and exploration of the parameter space by
300 combining resampling with subsequent Markov Chain Monte Carlo (MCMC) moves. Additionally, reflective boundaries are used to respect the predefined ranges of the prior uniform distributions. In our algorithm, we use 25,000 particles, a mini-batch size of 200 observations, and perform five MCMC steps per iteration step.

Due to the inherently stochastic nature of the SMC algorithm, different realizations can yield varying results. This variability arises from randomness in the prior sampling, the generation of proposals in each MCMC step, the selection of the mini-batches
305 of observations, and the determination of the m source locations representing the herd. As a result, it is common practice to run the SMC algorithm multiple times to (a) assess the variability of its output and (b) obtain more reliable statistical estimates of the inferred parameters (Chopin and Papaspiliopoulos, 2020; Vergé et al., 2015). Thereby, we perform 22 independent realizations of the SMC algorithm in an outer loop to derive more robust estimates of the CH_4 emission rates.

2.2.3 Mass balance method

310 The second drone-based method for quantifying CH_4 emission rates uses a mass balance approach. Based on the divergence theorem, this technique determines the emission rate from a CH_4 source by assessing the net horizontal inflow and outflow of CH_4 within an imaginary box enclosing the source. The mass balance approach, or box model, has been widely utilized with drone observations in various studies. For example, Allen et al. (2019) and Gålfalk et al. (2021) estimated emissions from landfills, while Andersen et al. (2021) determined emissions from coal mining ventilation shafts, and Vinković et al. (2022)
315 investigated emissions from a dairy farm. Additionally, Golston et al. (2018) and Yang et al. (2018) applied the mass balance method with a laser-based CH_4 sensor capturing a column-integrated concentration along a vertical path between the drone and the ground to investigate natural gas leaks. On larger scales, the method has been applied using aircraft observations. For example, Cambaliza et al. (2014) assessed emissions of an urban region including multiple sources such as power plants, landfills, and wastewater treatments, while Arndt et al. (2018) quantified emissions of dairy farms encompassing animal housing
320 and liquid manure storage. On regional or global scales, mass balance analysis is used to estimate emission rates from satellite



observations (e.g. Pandey et al. (2019); Borchardt et al. (2021)). However, Varon et al. (2018) notes that this method is susceptible to large errors. This is due to the inability to accurately parameterize turbulence on the small scale of instantaneous plumes, as well as poor characterization of the vertical wind speed profile between the ground surface and satellite.

The drone collects CH₄ point measurements along the vertical planes of an imaginary box encapsulating the source. Data are then interpolated onto a regular grid to calculate the net emission rate Q [g h⁻¹] by integrating the product of CH₄ concentration c [g m⁻³] and outward perpendicular wind speed across the vertical sampling planes:

$$Q = \sum_{\text{planes}} \left[\sum_i^{k_i} \sum_j^{k_j} c_{i,j} v_{\perp i,j} a_{i,j} \alpha \right], \quad (6)$$

where v_{\perp} [m s⁻¹] denotes the instantaneous wind speed outward perpendicular to the plane, a [m²] is the area of a grid cell, $\alpha = 3600$ s h⁻¹ is the time conversion factor from hours to seconds, k_i is the number of horizontal grid cells of a plane, and k_j is the number of vertical grid cells of a plane.

The vertical sampling planes must be sufficiently high to capture the full extent of the emissions, so that there are only negligible fluxes through the top horizontal plane of the imaginary box. Our imaginary box around the boma measures approximately 26 m by 26 m with a height of 10 m. To mitigate downwash effects from the rotors, the drone's flight plan was designed from the ground up. The drone first performed a manual flight at around 1.0 m above the ground for the lowest leg, followed by a pre-planned flight mission with ascending legs at approximately 2.0, 2.7, 3.7, 5.2, 7.2, and 9.2 m. The drone flew at 1 m s⁻¹, collecting observations approximately every meter. Figure 2 displays the measured CH₄ concentrations at a height of 2.7 m during the flight with the heifer herd on the same day as the satellite overpass.

To evaluate Eq. (6), we used the horizontal instantaneous corrected wind speed data from the drone and wind direction observations from the sonic anemometer on the flux tower, which we considered more reliable than the drone's wind direction estimates. Artificial wind speed data points of 0 m s⁻¹ were added at ground level to account for the no-slip lower boundary condition. The CH₄ concentration and perpendicular wind speeds were interpolated onto north-east (NE), south-east (SE), south-west (SW), and north-west (NW) facing vertical planes. Following the general approach of Gålfalk et al. (2021), we resampled the observations using the following sequence of steps: (a) linear interpolation of the data points onto a regular grid of circa 20 cm², (b) averaging onto a coarser grid of circa 1 m², and (c) filling any remaining empty grid cells, if any, using nearest-neighbor values.

The current sampling time of approximately 20 min is insufficient to capture the mean state of the plume morphology, introducing uncertainty into the emission rate estimate. This primarily stems from temporal variability induced by unresolved atmospheric turbulence affecting wind speed and wind direction ($\sigma_{v, \text{temp}}$ and $\sigma_{\phi, \text{temp}}$). This is further complicated by potential wake effects from the herd that disturb the mean flow field, influencing wind speed observations in the downwind sampling plane. Additionally, measurement uncertainties in wind speed and wind direction ($\sigma_{v, \text{meas}}$ and $\sigma_{\phi, \text{meas}}$) further contribute to the overall uncertainty in the mass balance approach. Moreover, the wind direction's assessment at the flux tower, rather than at the vertical planes, introduces additional uncertainty. The measurement uncertainty of the CH₄ observations is minimal and considered negligible compared to wind-related uncertainties. Similarly, the relative uncertainty of the interpolation process is



considered minor and is excluded from the overall uncertainty estimate. Our approach to uncertainty estimation for the mass
355 balance method aligns with the practices outlined in Andersen et al. (2021).

We estimate uncertainties due to temporal variation in wind speed and direction ($\sigma_{v, \text{temp}}$ and $\sigma_{\phi, \text{temp}}$) based on their standard
deviation from the mean at the altitude of each leg of the drone flight, following the methodology presented in Cambaliza et al.
(2014). Measurement uncertainties for wind speed and wind direction are estimated at $\sigma_{v, \text{meas}} = 1.7 \text{ m s}^{-1}$ and $\sigma_{\phi, \text{meas}} = 20^\circ$,
respectively. The wind speed uncertainty estimate is derived from the root mean square error between the corrected wind speed
360 readings from the drone and wind speed records from the sonic anemometer during hovering flights, see Sect. 2.2. The temporal
variation and measurement uncertainty are summed in quadrature: $\sigma_v = \sqrt{\sigma_{v, \text{temp}}^2 + \sigma_{v, \text{meas}}^2}$ and $\sigma_\phi = \sqrt{\sigma_{\phi, \text{temp}}^2 + \sigma_{\phi, \text{meas}}^2}$.
Finally, the total uncertainty estimate for the emission rate is determined through error propagation (Gålfalk et al., 2021;
Andersen et al., 2021; Vinković et al., 2022). A Monte Carlo approach with 500 runs is used for error propagation to incorporate
the various uncertainty sources.

365 2.3 IPCC Tier 2 emission values

In addition to drone-based methods, we estimate CH_4 emissions from enteric fermentation of ruminant herds at Kapiti using
the IPCC Tier 2 approach (Paustian et al., 2006). This method is based on the concept of energy balance, where the CH_4
emission factor EF [$\text{kg head}^{-1} \text{ d}^{-1}$] of ruminants is calculated by

$$EF = \frac{Y_m GE}{E}, \quad (7)$$

370 where Y_m denotes the fractional methane conversion factor, GE [$\text{MJ head}^{-1} \text{ d}^{-1}$] is the gross energy intake, and $E = 55.65 \text{ MJ kg}^{-1}$
is the energy content of CH_4 . The daily gross energy intake per animal GE is determined from information on feed quality and
feed intake, live weight of the animals, weight changes, as well as productivity parameters (as specified in Eq. 10.16 in Paustian
et al. (2006)). This data can be obtained at herd level, individual animal level, or a combination of both. Methane conversion
factor Y_m represents the fraction of gross energy intake converted to CH_4 . The IPCC provides Y_m values for different animal
375 categories based on review and synthesis of available scientific literature and data (cattle values in Table 10.12, and sheep and
goat values in Table 10.13 of Paustian et al. (2006)). Since specific values are currently unavailable for camels and we do not
have the live weight of the camel herd from our drone flights, we use the IPCC Tier 1 value for camels in our study.

At Kapiti, all livestock herds graze freely during the day, and we assume that their feed intake is entirely from pasture. The
feed quality of the pasture was determined by averaging the nutrient content of 19 samples collected from different locations
380 across Kapiti on 1 March 2024. These samples were analyzed for dry matter content, nitrogen (converted to crude protein),
carbon, ash, and fibre-fractions (NDF: Neutral Detergent Fibre; ADF: Acid Detergent Fibre; ADL: Acid Detergent Lignin).
This data was used to compute feed digestibility, representing the portion of gross energy intake in the feed not excreted in
feces. Data on average feed intake is difficult to obtain from grazing animals, and was therefore estimated.

The live weight [kg] and time-average daily live weight change [kg d^{-1}] of individual animals were determined from direct
385 measurements taken during the first half of March 2024, and then again at the end of April or May 2024. The average weight and
daily weight change across all animals in a herd were used to compute the EF for the respective animal category. Additional



390 data used to estimate gross energy intake for each animal herd includes: proportion of pregnant females (84% of pregnant does herd, 30% of cow herd, and 30% of slick herd); proportion of lactating females (87% of lactating ewes flock); with average milk production ($1.5 \text{ L ewe}^{-1} \text{ d}^{-1}$); number of offspring; and an estimate for the animal's activity, specifically the daily walking distance on the pasture [km d^{-1}]. We convert the resulting emission factor EF [$\text{kg head}^{-1} \text{ d}^{-1}$] into emission rate q [$\text{g head}^{-1} \text{ h}^{-1}$] for each animal category to enable method comparison in our study. With the exception of weight and weight changes, all parameters were estimated at the herd level without accounting for associated uncertainties. As we did not perform an explicit uncertainty assessment for the IPCC values, we apply a $\pm 20\%$ uncertainty range for Tier 2 values and a $\pm 30\%$ to $\pm 50\%$ uncertainty range for the Tier 1 value for camels, as reported by the IPCC (Paustian et al., 2006).

395 3 Results and discussion

In this section, we evaluate source location detection through satellite observations and assess each of the drone-based emission estimation methods. We then compare the estimated emission rates from the Bayesian inference method with the results obtained using the mass balance method and IPCC Tier 2 values. A comprehensive overview of the estimated emission rates by the different methods is given in Table B1.

400 3.1 Source detection through satellite observations

Figure 3 shows a true color image of part of Kapiti, captured by the PRISMA satellite on 6 March 2024. Despite the partly cloudy conditions, the irregular cloud cover did not occlude the satellite observations of all three cattle herds within our study area. Maps (c) to (e) show the SR index for a region of 5 by 5 pixels with a spatial resolution of 30m, across three different sites with (f) five adjacent bomas housing 583 cows, (g) the boma at the drone field site with 206 heifers, and (h) a free-grazing herd of 148 heifers, respectively.

We observe a lower SR index at the herd locations compared to the surrounding background. These low SR anomalies, which indicate relatively low radiance levels in the CH_4 absorption feature, may suggest higher atmospheric CH_4 concentrations and therefore point to the presence of a CH_4 source. The observed lower SR index precisely at the cattle herd locations illustrates the feasibility of using PRISMA satellite imagery to detect the location of potential CH_4 sources. In addition to CH_4 , bare soil exhibits unique features in the SWIR. We detected anomalies with two herds inside a boma against a bare soil background, and a free-grazing herd against a green vegetation background. Although the limited dataset prevents a robust assessment, these preliminary results reinforce our confidence in the effectiveness of our approach for detecting the location of potential CH_4 sources. Further dedicated studies are necessary to evaluate the generalizability of these findings.

Super-emitters are characterized by high concentration plumes with large spatial extents, often covering multiple pixels. In contrast, a low SR anomaly of a single pixel can be observed at the location of the cattle herds, as shown in Fig. 3. The absence of a discernible emission plume complicates the estimation of emission rates directly from the satellite data. While emission rates of super-emitters can be quantified from satellite images (Jacob et al., 2022), the current spatial resolution, spectral resolution and precision of satellite observations are insufficient for accurately estimating the emission rates of smaller

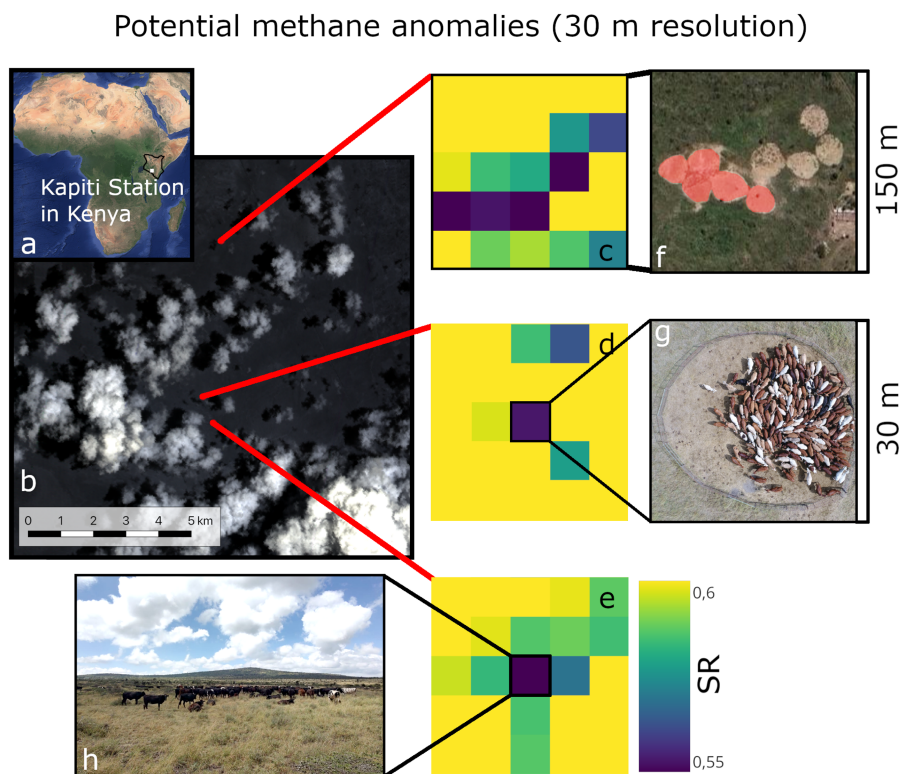


Figure 3. (a) Location of the field campaign at the Kapiti Research Station in Kenya. (b) PRISMA true color image of Kapiti from 6 March 2024 08:00 Coordinated Universal Time (UTC) + 3 hours, corresponding to East Africa Time. (c) to (e) The Simple Ratio (SR) radiance index of 2300/2100 nm with 30 m resolution for three distinct sites: (f) five adjacent bomas (shaded red) housing 583 cows at the time of the satellite overpass but empty in this picture, (g) a single boma at the drone field site with 206 heifers, and (h) a free-grazing herd of 148 heifers. (a) and (f) include © Google Satellite Imagery (2021). PRISMA product derived from L1 2024-03-06 ©Italian Space Agency (ASI) (2024). All rights reserved.

sources like livestock herds. The quantification threshold of point sources has been found to be 200 kg h^{-1} for GHGSat and $1,400 - 4,000 \text{ kg h}^{-1}$ for Sentinel-2, Landsat-8, PRISMA, and WorldView-3 in controlled release experiments under favorable conditions (Sherwin et al., 2023). In contrast, a herd of 200 cows emits considerably less, roughly $1 - 4 \text{ kg h}^{-1}$ (Broucek, 2014).

Detecting the location of potential CH_4 sources could represent a first step in mapping regional CH_4 sources. Such mapping can lay the groundwork for applying source term estimation methods, as targeted measurement campaigns can then focus on investigating these identified potential source locations. In our study with ruminant herds, the source locations are already known. However, this approach can be particularly useful for regions like thawing permafrost landscapes, where CH_4 source locations are generally unknown. Additional measurements are necessary to verify the location detection of potential CH_4



sources based on low SR anomalies and to quantify their emission rates. High-resolution observational platforms, such as drones, are needed to obtain the detailed data required to estimate CH₄ sources from livestock herds, such as those at Kapiti.

430 3.2 Source term estimation through drone observations

3.2.1 Bayesian inference method

In the atmospheric dispersion model given by Eq. (1), each of the meteorological parameters influences different aspects of the emission plume. Specifically, the wind direction determines the plume's orientation, while wind speed and diffusivity influence the plume's shape, and the emission rate determines how elevated the plume's concentration level is above the background. We consider these four parameters - wind direction ϕ , wind speed V , diffusivity D , and emission rate q - as
435 unknowns to be inferred. We compare Bayesian inference results across three observation cases: (a) using only concentration data, (b) combining concentration data with drone-derived wind speed, and (c) incorporating concentration data with mean wind direction, mean wind speed, and diffusivity obtained from MOST.

Figure 4 presents the Bayesian inference results for the drone flight conducted with the heifer herd on the afternoon of
440 6 March 2024, on the same day as the satellite overpass. Results for all drone flights are included in Fig. S4 to S24 of the Supplementary Material, and are reported in Table B1. In this section, we analyze the inference results, discussing the overall findings across all drone flights, and examine whether the results presented in Fig. 4 align with these overall findings.

In our study, we frequently observe different patterns when using drone-based methods to estimate CH₄ emission rates of sheep and goat herds at Kapiti compared to cattle herds. Except for camels, the herds consist of approximately 100 to 200
445 animals (see Table B1). Due to the markedly lower emission rate per individual animal q for sheep and goats, these herds have a lower overall emission rate Q . Consequently, we refer to the sheep and goat herds as 'weak(er) sources' to denote their relatively lower emission rates in our study.

In most of the drone flights, the inferred mean wind direction aligns with the fixed source location and areas of elevated concentration. Overall, the inferred wind direction is both precise and consistent across all three observation cases for cattle
450 drone flights, occasionally overriding the observed wind direction. In Fig. 4, the mean wind direction estimates across the three observation cases coincide, and the inferred direction of 81° corresponds to the angle between the source location and the observation locations with elevation concentration shown in Fig. 2. Specifically, the update in wind direction in observation case (a) indicates that our framework can often infer the wind direction solely from the shape of the concentration plume and the known source location. The posterior mean wind direction becomes more uncertain when dealing with highly variable wind
455 directions without direct observation (observation case (a)), such as during the morning flight with camels (Fig. S14) and the morning flight with pregnant does (Fig. S21).

For weak sources, the Bayesian inference algorithm can misinterpret concentration observations as being upwind of a strong emission source rather than downwind from a weak one if no direct wind direction observation is provided. To address this equifinality issue, we used an informed prior bounded by the half wind-rose: $\mathcal{U}(-45, 135)^\circ$. During the first two days of field
460 work, we used a narrower V-shaped flight path instead of the usual half-octagon. Consequently, for the drone flights on these

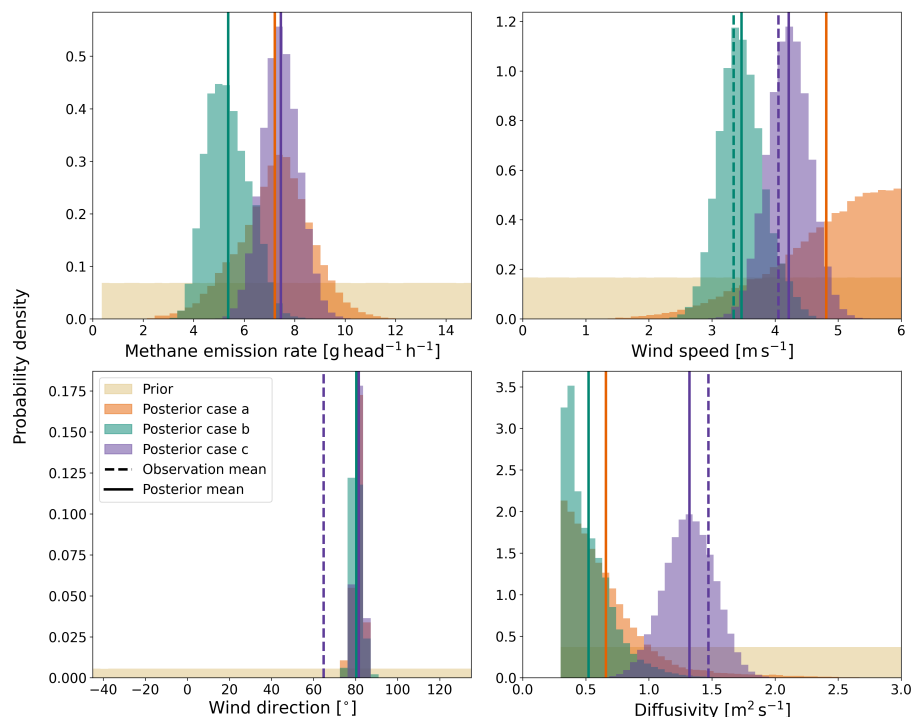


Figure 4. Bayesian inference results in the form of posterior distributions obtained using sequential Monte Carlo for the drone flight in the afternoon of 6 March 2024 with 208 heifers. Estimates for three different observation cases: (a) using concentration observations, (b) using concentration observations and mean wind speed data from the drone, (c) using concentration observations and mean wind speed, mean wind direction and diffusivity data derived from MOST.

days, marked with a bullet (•) in Table B1, we adjusted the prior to $\mathcal{U}(30, 135)^\circ$. When dealing with weak sources, an informed prior for wind direction was needed in our study to refine the emission rate distribution for observation cases without direct wind direction observations. Even with an informed prior, the posterior distribution of the wind direction can remain relatively uninformed for weak sources, such as weaner kids (Fig. S23 and S24). We note that concentration observations obtained in all
 465 locations around the source, such as those from the mass balance flight, can help mitigate this ambiguity.

Wind speed and diffusivity influence the shape of the emission plume. Higher wind speeds elongate the plume, while increased diffusivity broadens it. In observation cases (b) and (c), where direct wind speed observations are available, the posteriors generally align with these observed values. Typically, the wind speed derived from MOST (observation case (c)) is higher than the wind speed recorded by the drone (observation case (b)), as demonstrated in Fig. 4. Without direct wind speed
 470 observations (observation case (a)), the Bayesian inference algorithm tends to skew the posterior distribution toward higher wind speeds for most drone flights, as illustrated in Fig. 4. For all drone flights with weak sources, the wind speed posteriors for observation case (a) remain largely uninformed but are slightly skewed toward higher values.



For diffusivity, the posterior distribution in observation case (c) aligns with the direct observation, as shown in Fig. 4. In the absence of observations (observation cases (a) and (b)), the diffusivity posterior remains largely uninformed but slightly skewed toward higher values in drone flights with weaker sources as well as for the camel herd. For stronger sources, namely the cattle herds, the posterior distribution of diffusivity does often shift toward low values, as shown in Fig. 4.

A relationship was observed between the combination of high posterior wind speeds and high posterior diffusivity, resulting in higher estimated emission rates. Higher wind speed and diffusivity indicate a larger plume, both in length and width, suggesting a larger emission rate provided that the concentration observations are the same. The typically higher wind speeds derived from MOST, compared to drone wind speeds, combined with higher posterior diffusivity in observation case (c) compared to observation case (b), generally lead to higher emission rates in observation case (c) compared to observation case (b). This is demonstrated in Fig. 4. The observed relation highlights the importance of reliable wind measurements. We consider observation case (a) the least reliable, as the wind speed estimates often skew toward excessively high values. Observation cases (b) and (c) present an interesting topic for future study: Is it more valuable to have an anemometer on the drone to capture local and temporal wind variations, or to place an anemometer close to the source at a fixed location and use MOST to obtain diffusivity observations? Comparing different observing systems in controlled release experiments with a constant and known emission rate can provide further insights into the optimal experimental set-up for Bayesian inference observing systems.

Across all drone flights, the emission rate estimates for observation case (c) have a smaller relative uncertainty range compared to observation cases (a) and (b). Specifically, the range is approximately $\pm 50\%$ for strong sources and $\pm 12\%$ for weak sources, in contrast to $\pm 65\%$ and $\pm 26\%$ for observation case (a), and $\pm 55\%$ and $\pm 19\%$ for observation case (b), respectively.

We compare our estimates to IPCC Tier 1 values to assess their plausibility. It is important to note that IPCC Tier 1 values are highly uncertain, and we do not use these values as a definitive benchmark but rather as a sanity check. Overall, the Bayesian inference emission rate estimates for both strong and weak sources are of the same order of magnitude as the IPCC Tier 1 values: $5.3 \text{ g head}^{-1} \text{ h}^{-1}$ for dairy cattle in Africa, $5.3 \text{ g head}^{-1} \text{ h}^{-1}$ for camels in developing countries, and $0.6 \text{ g head}^{-1} \text{ h}^{-1}$ for sheep and goats in developing countries, with a reported uncertainty range of $\pm 30\%$ to $\pm 50\%$ (Paustian et al., 2006). Despite large variations in the posterior estimates for wind direction, wind speed, and diffusivity, the emission rate estimates across all observation cases remain consistent with these reference values. For example, for the drone flight presented in Fig. 4, the emission rate estimates of $7.2 \pm 1.4 \text{ g head}^{-1} \text{ h}^{-1}$, $5.4 \pm 0.8 \text{ g head}^{-1} \text{ h}^{-1}$, and $7.4 \pm 0.7 \text{ g head}^{-1} \text{ h}^{-1}$ for observation cases (a) to (c) respectively, are considered feasible when compared to the Tier 1 value for dairy cattle in Africa. This underscores the importance of reliable concentration observations, as they alone (observation case (a)) can provide reasonable emission rate estimates.

Further improvement of the Bayesian inference method could involve extending the sampling duration to more accurately capture the time-averaged plume. Prolonging the sampling time at each observation location may require modifications to the likelihood function. For example, Hutchinson et al. (2019) used a sample duration of 5 s and applied different likelihoods for concentration observations below and above a plume detection threshold. It is important to consider the trade-off between overall sampling duration and the number of sample locations. Investigating this trade-off, along with the formulation of the



likelihood function, would be a valuable area for future study to improve the Bayesian inference method for estimating CH₄ emission rates. Such optimization could maximize the informational value derived from observations collected with a single
510 battery set.

A promising approach to the information maximization strategy involves the use of autonomous drones that can make in-flight decisions about the optimal sampling path based on real-time observations and previously obtained knowledge. Several studies explore this possibility using reinforcement learning (Loisy and Eloy, 2022; van Hove et al., 2024b). However, these studies often rely on synthetic data, while research involving natural CH₄ sources under real-world conditions remains limited.
515 Instead of addressing the information maximization strategy solely on the data collection side, exploring the capabilities of Bayesian hierarchical modeling (Berliner, 2003) to enhance the utilization of information in future research is potentially valuable. The hierarchical Bayesian approach allows information to be shared across drone flights, enabling data to be pooled across, for example, the two heifer drone flights in this study, or across all drone flights involving cattle.

3.2.2 Mass balance method

520 Figure 5 presents the mass balance results of the afternoon drone flight with a herd of heifers, on the same day as the satellite overpass. The panels show the interpolated CH₄ concentrations (top), perpendicular wind speed (middle), and resulting fluxes (bottom) at the four vertical sampling planes in NE, SE, SW, and NW directions. The sum of the fluxes in the bottom panel equals the final estimated emission rate for the entire herd Q . The results of the other drone flights are included in Fig. S25 to S45 in the Supplementary Material, and Table B1.

525 Figure 2 demonstrates the intermittency of the observed instantaneous plume: the concentrations within the plume do not follow a smooth, continuous gradient but instead exhibit an irregular distribution of disconnected patches of high concentration. This intermittency complicates the mass balance approach, particularly for drone flights where the signal-to-noise ratio is relatively low. Such conditions include: (a) highly variable wind direction or low wind speeds leading to very non-stationary wind conditions (the noise is particularly high), and (b) drone flights with weaker emission sources resulting in low concentration levels (the signal is particularly low) where the variability in the background concentrations and emission plume can
530 considerably affect the accuracy of the emission rate estimate.

The mass balance approach relies on a nonzero horizontal wind to generate a horizontal outflow of CH₄ from the imaginary box. Its accuracy improves when the plume morphology remains relatively stable over time. Yang et al. (2018) defines favorable wind conditions as a wind speed greater than 2.3ms^{-1} and a steady wind direction with a standard deviation below 33.1° .
535 Measurements collected under wind conditions that do not meet these criteria are marked with a diamond (◆) in Table B1. These sub-optimal conditions lead to less reliable estimates, as for example observed by the negative mission rate of the morning drone flight with camels (Fig. S35). Consequently, these results should be considered unreliable due to unfavorable wind conditions.

Our observations indicate that the estimates for sheep and goats, marked by a triangle (▲) in Table B1, are very variable
540 and inconsistent with the IPCC Tier 1 value of $0.6\text{ghead}^{-1}\text{h}^{-1}$ (Paustian et al., 2006). Emissions from these smaller animals produce lower CH₄ concentration levels, resulting in a lower signal-to-noise ratio when considering the size of the herd. More-

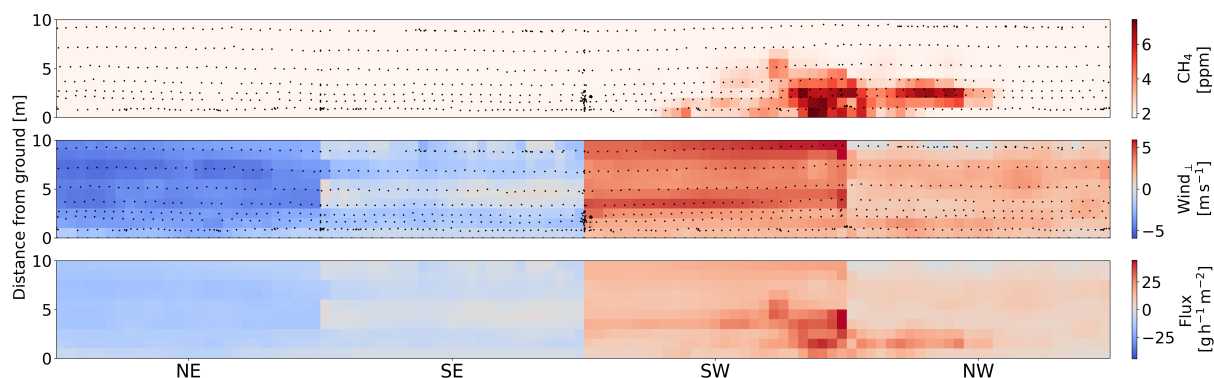


Figure 5. Results of the mass balance approach for a drone flight in the afternoon of 6 March 2024 with a herd of 208 heifers. The panels show (top) the interpolated CH₄ concentration observations, (middle) the interpolated perpendicular wind speeds, and (bottom) the CH₄ fluxes across the vertical sampling planes. Positive (negative) perpendicular wind speeds and fluxes correspond to flow out of (into) the box. The black scatter points indicate the original observation locations.

over, for sheep and goats, the emission source and consequently the plume, are close to the ground in a region characterized by generally lower wind speeds and complex surface effects caused by, for example, variations in elevation and vegetation. This may increase plume variability, leading to less reliable estimates. Due to these factors, we consider the mass balance estimates for drone flights with sheep and goats unreliable. The mass balance estimates for cattle are more plausible, as they are of the same order of magnitude as the IPCC Tier 1 value of 5.3 g head⁻¹ h⁻¹ for dairy cattle in Africa (Paustian et al., 2006). The negative emission rate for camels in the morning is unrealistic, but the estimate in the afternoon is within a similar range as the IPCC Tier 1 value of 5.3 g head⁻¹ h⁻¹ (Paustian et al., 2006).

To mitigate the effect of plume variability over time, several studies have conducted repeated drone flights (Gålfalk et al., 2021; Andersen et al., 2021). In the absence of systematic bias, this approach can yield a more robust approximation of the emission rate by averaging the estimates from multiple drone flights, thereby reducing - though not eliminating - uncertainty due to temporal variability. In a single drone flight, capturing the time-averaged plume can potentially be improved by increasing the number of plume observations relative to background observations. Several studies, particularly larger-scale experiments using airplanes, conduct flights along a single vertical sampling plane downwind from the prevailing wind direction (Allen et al., 2019; Cambaliza et al., 2014). The term $c_{i,j}$ in Eq. (6) is then replaced by $c_{i,j} - c_0$, where c_0 is the estimated background concentration. However, this sampling approach introduces uncertainty due to the estimation of the background concentration, whose variability must be accounted for in the overall uncertainty estimate.

Although onboard wind measurements with a sonic anemometer are considered ideal (Allen et al., 2019), practical constraints have necessitated the use of nearby weather stations for wind data in several studies (Allen et al., 2019; Nathan et al., 2015). Morales et al. (2022) demonstrated through controlled release experiments that using wind data from an anemometer close to the source, which captures changing wind conditions during the flight, is more accurate than applying a wind profile through MOST (Eq. (A1)) that only accounts for wind speed variation with altitude. Given that we did not have an anemome-



565 ter available on the drone, using corrected wind speeds from the flight controller was our best available option. An onboard
anemometer could reduce measurement uncertainty of the instantaneous wind field, but it does not reduce uncertainty due to
temporal uncertainty.

3.3 Method comparison

In this section, we evaluate the CH₄ emission rate results obtained using the Bayesian inference method by comparing them to
the results derived from other methods and literature values. Figure 6 presents the Bayesian inference results for observation
case (c) alongside estimates from the mass balance approach, a laser spectrometry study previously conducted at Kapiti by Wolz
570 et al. (2022), and the IPCC emission values.

In Sec. 3.2.1 and 3.2.2, we observed that the Bayesian inference results for all herds are of the same order of magnitude as
the IPCC Tier 1 values. Conversely, while our mass balance results for strong sources (cattle herds) are within the same order
of magnitude as the IPCC Tier 1 values, they are substantially higher than the IPCC Tier 1 values for weak sources (sheep and
goat herds) for a majority of drone flights. This finding is further supported by comparison to the herd-specific IPCC Tier 2
575 values. We observe that both the Bayesian inference and mass balance results are in the same order of magnitude as the IPCC
Tier 2 values for strong sources of $Q \approx 700 \text{ g h}^{-1}$ to $Q \approx 1,500 \text{ g h}^{-1}$ (Table B1). However, a majority of the mass balance
results are substantially higher than the IPCC Tier 2 values for weaker sources of $Q \approx 70 \text{ g h}^{-1}$ to $Q \approx 140 \text{ g h}^{-1}$ (Table B1).
This inconsistency indicates that the source term estimation threshold of the Bayesian inference method is considerably lower
than that of the mass balance method as applied in our study, suggesting that Bayesian inference can be used to estimate weaker
580 sources, where the mass balance method might fail to reliably estimate sources.

We compare the Bayesian inference estimates to results from previous studies conducted at Kapiti. Our average (pre-
and post-grazing) emission rate estimate for steers was $7.1 \pm 0.7 \text{ g h}^{-1}$, which aligns with a respiration chamber experiment
showing emission rates ranging from $6.7 - 7.7 \text{ g head}^{-1} \text{ h}^{-1}$ depending on diet (Korir et al., 2022b). Our average emission
rate estimate for lactating ewes was $0.8 \pm 0.2 \text{ g head}^{-1} \text{ h}^{-1}$, which overlaps with the emission rate for sheep ranging from
585 $0.6 - 0.8 \text{ g head}^{-1} \text{ h}^{-1}$ found in a respiration chamber experiment (Mwangi et al., 2023). Our estimate is on the higher end,
which is expected as emissions from lactating animals are generally larger than those from non-lactating animals due to their
increased feed intake to meet the energy demands of milk production (Broucek, 2014). In another respiration chamber experi-
ment, the estimated emission rates from cows ranged from $7.6 - 11.3 \text{ g head}^{-1} \text{ h}^{-1}$ depending on diet (Korir et al., 2022a). In
contrast, our average estimate was notably higher at $15.2 \pm 1.0 \text{ g head}^{-1} \text{ h}^{-1}$.

590 Wolz et al. (2022) utilized open-path laser spectroscopy with backward Lagrangian stochastic dispersion modeling to esti-
mate nighttime CH₄ emissions from a mixed cattle herd across 14 nights in September and October 2019. The resulting mean
emission rates Q were normalized to the equivalent weight of a cow to obtain q for a hypothetical cow herd, rather than nor-
malizing by the number of animals to obtain q for the observed mixed cattle herd. Figure 6 shows the results obtained at 09:00
East Africa Time (EAT), before grazing, and at 00:30 EAT, after grazing. Note that the latter nocturnal measurements were
595 obtained later than our drone flights, which were conducted in the afternoon. We observe that our Bayesian inference results
for cows are higher, both before and after grazing, compared to estimates from Wolz et al. (2022). This discrepancy could be

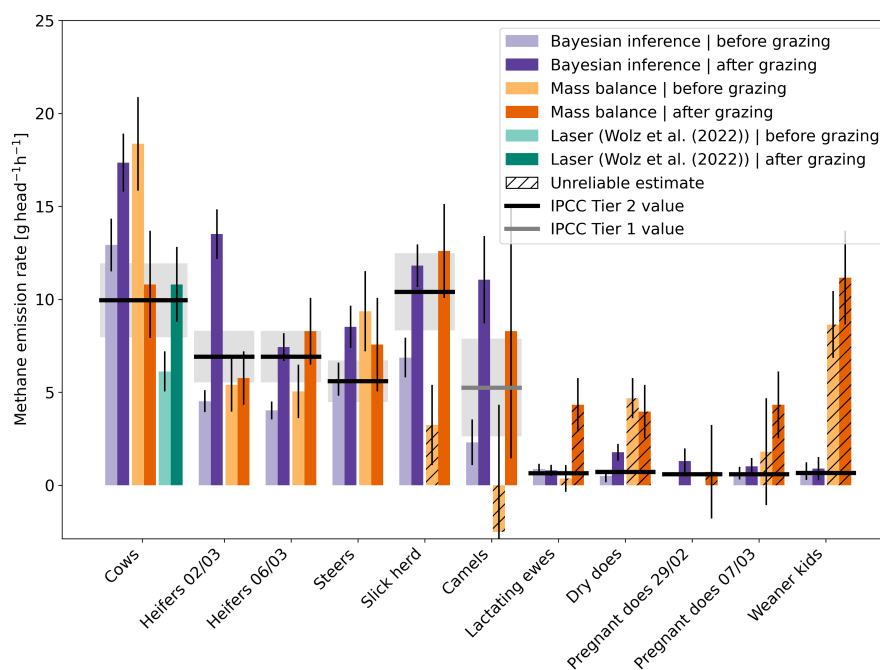


Figure 6. Methane emission rate estimates from the Bayesian inference method using concentration observations and mean wind speed, mean wind direction, and diffusivity data derived from Monin Obukhov Similarity Theory (observation case (c)), the mass balance approach, a laser spectrometry study by Wolz et al. (2022), and IPCC emission values. Error bars represent one standard deviation uncertainty. The uncertainty range of IPCC values, depicted by gray shading, is $\pm 20\%$ for Tier 2 values and $\pm 30\%$ to $\pm 50\%$ for Tier 1 values (Paustian et al., 2006), this figure uses $\pm 50\%$ for the IPCC Tier 1 value. Unreliable mass balance estimates due to a low signal-to-noise ratio are indicated by hatched lines.

due to an overestimation by the Bayesian inference method, or the emission rate might have been this high at the times of the drone flights. Wolz et al. (2022) reported a mean emission rate over 14 repeated experiments, whereas the Bayesian inference result is an estimate based on a single drone flight. Additionally, differences in methodology, differences in the timing of the measurements, and the herd weight normalization used by Wolz et al. (2022) could contribute to the variance. Both studies were conducted at the end of a dry season; however, our field campaign was conducted during a normal dry season, whereas the dry season studied by Wolz et al. (2022) was extreme. The severity of this dry season likely affected feed intake and feed quality, potentially reducing CH_4 emission rates.

No camel studies have previously been conducted in Kapiti, so we compared our Bayesian inference results for camels to those of a respiration chamber experiment conducted in Australia by Dittmann et al. (2014). This study estimated a CH_4 emission rate of $4.0 \text{ g head}^{-1} \text{ h}^{-1}$ for Bactrian camels fed exclusively on alfalfa. Our average (pre- and post-grazing) estimate is higher at $6.7 \pm 1.3 \text{ g head}^{-1} \text{ h}^{-1}$. Note that the studies involve different camel species and diets. Our average estimate aligns better with the IPCC Tier 1 value of $5.3 \text{ g head}^{-1} \text{ h}^{-1}$. We emphasize that the number of experiments conducted with camels



and the extent of current knowledge are minimal, and that further research is required to gain more insight into the emissions
610 of CH₄ from camels. Based on Bayesian inference, we observe a larger increase in estimated CH₄ production after grazing in
camels compared to cattle. Replication of this result through repeated experiments would be a promising avenue for further
research.

Feeding is known to increase CH₄ production in ruminants (Amon et al., 2001; Hegarty, 2013), and we assess whether this
effect is observable in our results for the other herds as well. The Bayesian inference results show the hypothesized effect of
615 grazing in seven out of ten cases, with considerably higher emission rate estimates in the afternoon compared to the morning.
In the cases of pregnant does and weaner kids, although there is a general increase in emission estimates before and after
grazing, the considerable overlap in the uncertainty ranges makes the effect less clear. For the final case of lactating ewes, the
difference in emissions before and after grazing is slightly negative; however, the uncertainty ranges overlap, making the effect
inconclusive. In contrast, the mass balance results do not consistently demonstrate an increase in CH₄ emissions post-grazing,
620 with a substantial increase observed in only three out of ten cases - heifers 06/03, slick herd, and lactating ewes. We consider
this to be a promising indicator for the greater reliability and accuracy of our Bayesian inference results compared to our mass
balance results.

With the exception of the cows and lactating ewes drone flights, the Bayesian inference estimates pre-grazing are lower than
the IPCC Tier 2 value, and the post-grazing estimates are higher than the IPCC Tier 2 value, or the uncertainty ranges of the
625 different methods overlap. One advantage of using the Bayesian inference method over the IPCC Tier 2 approach is the ability
to estimate diurnal variations, which allows us to observe the effects of feeding. Additionally, the uncertainty in the Bayesian
inference results can typically be reduced by assimilating a larger dataset, suggesting that repeated drone flights can yield more
reliable results (Pirk et al., 2022). Deriving IPCC Tier 2 values is time-consuming due to the measurement of live weight and
live weight changes of individual animals, and considerable unquantified uncertainty remains in our ability to estimate the feed
630 intake of animals in pastoral systems like at Kapiti. Furthermore, the accuracy of the method relies partly on the accuracy of the
methane conversion factor Y_m , which is determined based on previous research and may not be representative of the specific
animals being studied.

In comparison to the Bayesian inference method, the mass balance approach is more straightforward to implement. However,
based on this study, Bayesian inference results can be more reliable, as demonstrated by the consistent observation of increased
635 emissions post-grazing. In both the mass balance method and the Bayesian inference method, we use a sensor - a drone -
to capture snapshots of a non-stationary emission plume. However, the physical models of both methods - Eq. (1) for our
Bayesian inference approach and Eq. (6) for the mass balance method - are based on the assumption of a statistically stationary
plume. A conceptual difference between the two methods lies in how they handle the discrepancy between the turbulent
(instantaneous) observations acquired by the drone and the mean concentration and mean wind field represented in the model.
640 The Bayesian inference method explicitly accounts for this discrepancy through observation error \mathbf{R} , while the mass balance
approach does not explicitly address this inconsistency. Instead, we only account for this violation implicitly by including
a temporal variation term within the uncertainty range of the mass balance estimates. We observed that the mass balance
approach estimates are sensitive to low signal-to-noise levels, making the resulting estimates of weaker sources and under



highly variable wind conditions unreliable. In contrast, the Bayesian inference method proved to be more robust in estimating
645 weaker sources and under variable wind conditions. This robustness may be attributed to explicitly accounting for discrepancies
between instantaneous observations and the assumed stationarity of the concentration and wind fields in the physical model.

4 Conclusions

In our study, we leveraged drone and flux tower observations along with a Bayesian inference approach to quantify CH₄ emis-
sions of ruminants in sub-Saharan Africa - an important, yet poorly understood, source in the global CH₄ emission inventory.
650 We showed how this method can be applied to verify and estimate potential CH₄ sources identified through radiance anomalies
observed in hyperspectral satellite data.

4.1 Bayesian lessons learned

While Bayesian inference is regularly applied on regional and global scales to detect and estimate carbon emissions using
satellite observations and international sensor networks, its application on smaller spatial scales with weaker sources, such as
655 the livestock herds in our study, is limited. Our work demonstrates the feasibility and effectiveness of using Bayesian inference
methods with drone and flux tower observations for source term estimation on local scales. Here, we share our experiences in
quantifying CH₄ emissions using this approach, with the aim of advancing research in local source term estimation through
Bayesian inference.

Rather than treating the herd as a single point source, we modeled it as a set of sources with equal strengths, which we found
660 to be more accurate. Modeling the herd as a single point source led to higher inferred mean diffusivity in most drone flights
due to the large horizontal spread of instantaneous observed elevated concentrations above background level.

We assumed the set of source locations to be fixed known parameters. When treated as an unknown parameter, the posterior
distribution for source location broadened along the prevailing wind direction and increased the uncertainty in the emission rate
estimates. This can be attributed to equifinality: a stronger source further away can produce a similar concentration observation
665 as a weaker source nearby. Incorporating concentration data collected around the source enhanced the accuracy of source
location posteriors. We tested this by incorporating the observations of the mass balance flights.

We observed equifinality across multiple parameter combinations, implying that incorporating observations related to un-
known parameters is beneficial and may even be necessary to adequately constrain their probability distributions. While wind
direction can be effectively constrained using concentration observations alone, wind speed measurements - such as those from
670 the drone or flux tower - considerably enhanced the inference process. Further research is recommended to identify the most
reliable observational platform for this purpose. Diffusivity proved difficult to constrain based on instantaneous concentration
observations alone, but we observed that diffusivity observations derived from eddy-covariance data helped to constrain the
diffusivity probability distribution.

We restricted the uniform prior for wind direction to a half wind-rose aligned with the prevailing wind direction. Using the
675 entire wind-rose introduced ambiguity between upwind observations of strong sources and downwind observations of weak



sources, specifically in drone flights with herds of sheep and goats. Incorporating concentration observations around the source can help mitigate this ambiguity.

680 Treating the background concentration as a known parameter was necessary in this study because the Bayesian inference algorithm struggled to infer reliable estimates in several drone flights when this parameter was considered unknown, leading to unreliable emission rate inferences. The algorithm struggled to distinguish between background and elevated concentrations without relying on this assumption. We anticipate that using concentration observations obtained over longer sampling times, with an adjusted likelihood function, could potentially address this issue.

685 The biggest challenge in setting up the Bayesian framework in our study was the mismatch between instantaneous concentration observations and the time-averaged dispersion model, which complicated the design of the likelihood function. A broad Gaussian likelihood proved effective. Still, we recommend further investigation into the likelihood design, in combination with extended sampling times to better capture the time-averaged emission plume. However, longer sampling times reduce the number of locations that can be observed on a single drone battery charge. This limitation makes intelligent sampling path design a promising topic for further study.

4.2 Insights into CH₄ emission detection and estimation from ruminants

690 By analyzing radiance anomalies in hyperspectral PRISMA satellite data, we detected three cattle herds present at Kapiti Research Station in Kenya. Using the ratio between radiance in the 2300 nm and 2100 nm bands, we showed that it is feasible to locate herds within a boma and free-grazing herds. In particular, this approach allows us to identify the location of potential CH₄ sources emitting approximately 1,000 g h⁻¹ or more. While the detection of the location of potential CH₄ sources, such as cattle herds, is feasible using current satellite data, higher-resolution observations are necessary to accurately estimate their CH₄ emission rates.

700 Using drone observations, we estimated the CH₄ emission rates of various ruminant herds - including cattle (cows, heifers, steers, and slick herd), sheep (lactating ewes), goats (dry does, pregnant does, weaner kids), and camels - by applying both Bayesian inference and mass balance approaches. Due to low signal-to-noise levels, the mass balance method did not consistently provide reliable estimates for weaker sources, such as the sheep and goat herds. However, under favorable wind conditions, we estimated cattle herd emissions ranging between 700 – 1,500 g h⁻¹ using the mass balance method. The Bayesian inference method performed better for weaker sources, estimating sheep and goat herd emissions in the range of 70 – 140 g h⁻¹, and it was effective for the different cattle and camel herds as well.

705 We observed the hypothesized increase in CH₄ production following feeding in a majority of the Bayesian inference drone flights, whereas this effect was visible in only a minority of the mass balance flights. Additionally, the Bayesian inference method results appeared less affected by variable wind conditions than the mass balance method. These observations suggest the superior performance of the Bayesian inference method over the mass balance method in this setting.

Overall, the Bayesian inference results aligned with the IPCC Tier 2 emission values. Compared to the IPCC Tier 2 approach, the Bayesian inference method offers the ability to estimate temporal variations in CH₄ production. Furthermore, the method can assimilate observations from various measurement platforms and incorporate their uncertainties. The strong performance



710 of the Bayesian inference approach in this case study, estimating diverse CH₄ source strengths under various atmospheric conditions, underscores its robustness and potential as a valuable method for estimating CH₄ sources in agricultural areas and other landscapes.

4.3 Future applications

715 We demonstrated the potential of the Bayesian inference method to estimate a range of source strengths. Specifically, we showed that potential CH₄ sources detected by hyperspectral satellites, but too weak to be confidently quantified, can be effectively estimated using drone observations. Future applications of the Bayesian framework for source term estimation could extend to diverse natural and anthropogenic sources, such as CH₄ emissions from wetlands, hotspots in thawing permafrost, landfills, and wastewater disposal sites.

720 In areas where observational data are sparse, the Bayesian inference method can be employed using a gas sensor and an anemometer mounted on the drone or positioned near the source. This approach could eliminate the need for a nearby flux tower, making the observing framework suitable for remote sites. Conversely, in observation-rich environments, the Bayesian inference method can integrate data from multiple observation platforms. For example, data obtained from laser spectrometry or observations from multiple drones can be assimilated.

725 Overall, the insights gained in our study demonstrate the potential of Bayesian inference methods, combined with drone and flux tower observations, for improving our understanding of CH₄ emissions at local scales, thereby contributing to the improvement of CH₄ inventories and mitigation studies.

Code and data availability. The drone and flux tower data set, along with the Digital Elevation Model of Kapiti, can be accessed from van Hove et al. (2024a). The data processing scripts are available at <https://github.com/AlouetteUiO/MIK>.

Appendix A: MOST

730 Obukhov length L [m] is positive in stable atmospheric conditions and negative in unstable atmospheric conditions. During all drone flights, the atmosphere was unstable. We use Monin Obukhov Similarity Theory (MOST; see Stull, 1989; Hanna et al., 1982) to estimate the vertical profile of the mean wind speed $V(z)$ [m s⁻¹] and mean eddy diffusivity $K(z)$ [m² s⁻¹], where z is the distance above the ground.

Under unstable atmospheric conditions, the mean wind speed profile is estimated by

$$735 \quad V(z) = \frac{u_*}{\kappa} \left[\ln \left(\frac{z-d}{z_0} \right) - 2 \ln \left(\frac{1}{2} \left(1 + \frac{1}{\Phi_M} \right) \right) - \ln \left(\frac{1}{2} \left(1 + \frac{1}{\Phi_M^2} \right) \right) + 2 \arctan \left(\frac{1}{\Phi_M} \right) - \frac{\pi}{2} \right], \quad (\text{A1})$$

where u_* is the friction velocity, $\kappa = 0.4$ is the von Kármán constant, and z_0 [m] is the aerodynamic roughness length. We use $z_0 = 0.05$ m, which corresponds to terrain with long grass and few trees (Stull, 1989), and a displacement height of $d = 0.10$ m.



The dimensionless wind shear Φ_M is approximated by

$$\Phi_M \left(\frac{z}{L} \right) = \left[1 - 15 \frac{z-d}{L} \right]^{-1/4}. \quad (\text{A2})$$

740 The resulting mean wind speed at the height of the sonic anemometer on the flux tower qualitatively matches the mean wind speeds measured by the same sonic anemometer (Fig. S3 in Supplementary Material).

The eddy diffusivity for effectively passive tracers such as CH_4 is generally assumed to be equal to the eddy diffusivity for heat. The mean eddy diffusivity profile is given by

$$K(z) = \kappa u_* \frac{z-d}{\Phi_H}, \quad (\text{A3})$$

745 where Φ_H is the dimensionless potential temperature gradient. For unstable atmospheric conditions, it is assumed to be given by

$$\Phi_H \left(\frac{z}{L} \right) = 0.74 \left[1 - 9 \frac{z-d}{L} \right]^{-1/2}. \quad (\text{A4})$$

Appendix B: Results table

Author contributions. Conceptualization: AvH, NP, KA. Methodology: AvH, KA, NP. Software: AvH. Formal analysis: AvH (drone-based methods), VL (IPCC Tier 2 values), RC (satellite data). Investigation: AvH and JH (drone flights), VO (eddy-covariance data), RC and FF (satellite data). Resources: CA (host at Kapiti and coordination field campaign). Writing - Original Draft: AvH. Writing - Review & Editing: KA, NP, VL, CA, RC, VO, FF, AvH. Visualization: AvH, RC (Fig. 3). Funding acquisition: VL, NP.

Competing interests. The authors declare that they have no conflict of interest.

Acknowledgements. We would like to thank Ilona Gluecks from ILRI for providing information about the different ruminant herds at Kapiti, and Endale Balcha Gurmu from ILRI for assisting with the IPCC Tier 2 workflow. Furthermore, we would like to thank Nehemiah Kimengich, Nelson Kipchirchir and Elly Kibira at Kapiti for their assistance in the field. Moreover, we would like to thank Luc Girod from UiO for his help with drone imagery processing. This study contains modified data of the PRISMA satellite of ESA - Agenzi Spaziale Italiana (ASI) [Year 2024]. We would like to thank Monica Pepe from CNR and Patrizia Sacco from ASI for the data procurement. This work was supported by the Research Council of Norway (projects #333232 (CircAgric-GHG) and #301552 (Spot-On)) and the European Research Council (project #101116083 (ACTIVATE)). This work is a contribution to the strategic research initiative LATICE (#UiO/GEO103920), the Center for Biogeochemistry in the Anthropocene, as well as the Center for Computational and Data Science at the University of Oslo. This study was supported by the CGIAR Initiatives Livestock and Climate and Mitigate+: Low-Emission Food Systems, which are supported by contributors

<https://doi.org/10.5194/egusphere-2024-3994>

Preprint. Discussion started: 9 January 2025

© Author(s) 2025. CC BY 4.0 License.



to the CGIAR Trust Fund. This work was supported by the European Union through the EU-DeSIRA ESSA project (Earth observation and environmental sensing for climate-smart sustainable agropastoralism ecosystem transformation in East Africa). The content of this article is
765 the sole responsibility of the authors and does not necessarily reflect the views of the European Union.



References

- Abichandani, P., Lobo, D., Ford, G., Bucci, D., and Kam, M.: Wind Measurement and Simulation Techniques in Multi-Rotor Small Unmanned Aerial Vehicles, *IEEE Access*, 8, 54 910–54 927, <https://doi.org/10.1109/ACCESS.2020.2977693>, 2020.
- Allen, G., Hollingsworth, P., Kabbabe, K., Pitt, J. R., Mead, M. I., Illingworth, S., Roberts, G., Bourn, M., Shallcross, D. E., and Percival, C. J.: The development and trial of an unmanned aerial system for the measurement of methane flux from landfill and greenhouse gas emission hotspots, *Waste Management*, 87, 883–892, <https://doi.org/10.1016/j.wasman.2017.12.024>, 2019.
- Amon, B., Amon, T., Boxberger, J., and Alt, C.: Emissions of NH₃, N₂O and CH₄ from dairy cows housed in a farm-yard manure tying stall (housing, manure storage, manure spreading), *Nutrient Cycling in Agroecosystems*, 60, 103–113, <https://doi.org/10.1023/A:1012649028772>, 2001.
- Andersen, T., Vinkovic, K., De Vries, M., Kers, B., Necki, J., Swolkien, J., Roiger, A., Peters, W., and Chen, H.: Quantifying methane emissions from coal mining ventilation shafts using an unmanned aerial vehicle (UAV)-based active AirCore system, *Atmospheric Environment: X*, 12, 100 135, <https://doi.org/10.1016/j.aeaoa.2021.100135>, 2021.
- Arndt, C., Leytem, A., Hristov, A., Zavala-Araiza, D., Cativiela, J., Conley, S., Daube, C., Faloona, I., and Herndon, S.: Short-term methane emissions from 2 dairy farms in California estimated by different measurement techniques and US Environmental Protection Agency inventory methodology: A case study, *Journal of Dairy Science*, 101, 11 461–11 479, <https://doi.org/10.3168/jds.2017-13881>, 2018.
- Bai, M., Velazco, J. I., Coates, T. W., Phillips, F. A., Flesch, T. K., Hill, J., Mayer, D. G., Tomkins, N. W., Hegarty, R. S., and Chen, D.: Beef cattle methane emissions measured with tracer-ratio and inverse dispersion modelling techniques, *Atmospheric Measurement Techniques*, 14, 3469–3479, <https://doi.org/10.5194/amt-14-3469-2021>, 2021.
- Baldwin, R., McLeod, K., Klotz, J., and Heitmann, R.: Rumen Development, Intestinal Growth and Hepatic Metabolism In The Pre- and Postweaning Ruminant, *Journal of dairy science*, 87, E55–E65, 2004.
- Banner, K. M., Irvine, K. M., and Rodhouse, T. J.: The use of Bayesian priors in Ecology: The good, the bad and the not great, *Methods in Ecology and Evolution*, 11, 882–889, <https://doi.org/10.1111/2041-210X.13407>, 2020.
- Berliner, L. M.: Physical-statistical modeling in geophysics, *JOURNAL OF GEOPHYSICAL RESEARCH*, 108, 8776, <https://doi.org/10.1029/2002JD002865>, 2003.
- Borchardt, J., Gerilowski, K., Krautwurst, S., Bovensmann, H., Thorpe, A. K., Thompson, D. R., Frankenberg, C., Miller, C. E., Duren, R. M., and Burrows, J. P.: Detection and quantification of CH₄ plumes using the WFM-DOAS retrieval on AVIRIS-NG hyperspectral data, *Atmospheric Measurement Techniques*, 14, 1267–1291, <https://doi.org/10.5194/amt-14-1267-2021>, 2021.
- Broucek, J.: Production of Methane Emissions from Ruminant Husbandry: A Review, *Journal of Environmental Protection*, 05, 1482–1493, <https://doi.org/10.4236/jep.2014.515141>, 2014.
- Brown, L. R., Benner, D. C., Champion, J. P., Devi, V. M., Fejard, L., Gamache, R. R., Gabard, T., Hilico, J. C., Lavorel, B., Loete, M., Mellau, G. C., Nikitin, A., Pine, A. S., Predoi-Cross, A., Rinsland, C. P., Robert, O., Sams, R. L., Smith, M. A., Tashkun, S. A., and Tyuterev, V. G.: Methane line parameters in HITRAN, *Journal of Quantitative Spectroscopy and Radiative Transfer*, 82, 219–238, [https://doi.org/10.1016/S0022-4073\(03\)00155-9](https://doi.org/10.1016/S0022-4073(03)00155-9), 2003.
- Burba, G.: Eddy Covariance Method for Scientific, Industrial, Agricultural and Regulatory Applications: A Field Book on Measuring Ecosystem Gas Exchange and Areal Emission Rates, *LI-COR Beosciences*, ISBN 978-0-615-76827-4, <https://doi.org/10.13140/RG.2.1.4247.8561>, 2013.

Burgués, J. and Marco, S.: Environmental chemical sensing using small drones: A review, *Science of The Total Environment*, 748, 141–172, <https://doi.org/10.1016/j.scitotenv.2020.141172>, 2020.

805 Busetto, L. and Ranghetti, L.: prismaread: A tool for facilitating access and analysis of PRISMA L1/L2 hyperspectral imagery v1. 0.0, URL: <https://busett.github.io/prismaread/https://doi.org/10.5281/zenodo.4019081>, 2020.

Calder, K. L.: Multiple-source plume models of urban air pollution—their general structure, *Atmospheric environment*, 11, 403–414, 1977.

810 Cambaliza, M. O. L., Shepson, P. B., Caulton, D. R., Stirm, B., Samarov, D., Gurney, K. R., Turnbull, J., Davis, K. J., Possolo, A., Karion, A., Sweeney, C., Moser, B., Hendricks, A., Lauvaux, T., Mays, K., Whetstone, J., Huang, J., Razlivanov, I., Miles, N. L., and Richardson, S. J.: Assessment of uncertainties of an aircraft-based mass balance approach for quantifying urban greenhouse gas emissions, *Atmospheric Chemistry and Physics*, 14, 9029–9050, <https://doi.org/10.5194/acp-14-9029-2014>, 2014.

Chopin, N.: A sequential particle filter method for static models, *Biometrika*, 89, 539–552, <https://doi.org/10.1093/biomet/89.3.539>, 2002.

Chopin, N. and Papaspiliopoulos, O.: *An Introduction to Sequential Monte Carlo*, Springer Series in Statistics, Springer Nature, Cham, 1st edition 2020 edn., ISBN 9783030478452, 2020.

815 Crazzolara, C., Ebner, M., Platis, A., Miranda, T., Bange, J., and Junginger, A.: A new multicopter-based unmanned aerial system for pollen and spores collection in the atmospheric boundary layer, *Atmospheric Measurement Techniques*, 12, 1581–1598, <https://doi.org/10.5194/amt-12-1581-2019>, 2019.

Cusworth, D. H., Bloom, A. A., Ma, S., Miller, C. E., Bowman, K., Yin, Y., Maasackers, J. D., Zhang, Y., Scarpelli, T. R., Qu, Z., Jacob, D. J., and Worden, J. R.: A Bayesian framework for deriving sector-based methane emissions from top-down fluxes, *Communications Earth & Environment*, 2, 242, <https://doi.org/10.1038/s43247-021-00312-6>, 2021.

820 Daube, C., Conley, S., Faloona, I. C., Arndt, C., Yacovitch, T. I., Roscioli, J. R., and Herndon, S. C.: Using the tracer flux ratio method with flight measurements to estimate dairy farm CH₄ emissions in central California, *Atmospheric Measurement Techniques*, 12, 2085–2095, <https://doi.org/10.5194/amt-12-2085-2019>, 2019.

Dittmann, M. T., Runge, U., Lang, R. A., Moser, D., Galeffi, C., Kreuzer, M., and Clauss, M.: Methane Emission by Camelids, *PLoS ONE*, 9, e94363, <https://doi.org/10.1371/journal.pone.0094363>, 2014.

825 Dogniaux, M., Maasackers, J. D., Varon, D. J., and Aben, I.: Report on Landsat 8 and Sentinel-2B observations of the Nord Stream 2 pipeline methane leak, *Atmospheric Measurement Techniques*, 17, 2777–2787, <https://doi.org/10.5194/amt-17-2777-2024>, 2024.

Doucet, A. and Johansen, A. M.: A Tutorial on Particle Filtering and Smoothing: Fifteen years later, *Handbook of Nonlinear Filtering*, 12, 2009.

830 Evangeliou, N., Thompson, R. L., Eckhardt, S., and Stohl, A.: Top-down estimates of black carbon emissions at high latitudes using an atmospheric transport model and a Bayesian inversion framework, *Atmospheric Chemistry and Physics*, 18, 15307–15327, <https://doi.org/10.5194/acp-18-15307-2018>, 2018.

Francis, A., Li, S., Griffiths, C., and Sienz, J.: Gas source localization and mapping with mobile robots: A review, *Journal of Field Robotics*, <https://doi.org/10.1002/rob.22109>, 2022.

835 Gavrilova, O., Leip, A., Dong, H., Macdonald, J., Gomez, C., Amon, B., Barahona Rosales, R., Agustin, Del Prado, A., Lima, M., Oyhantcabal, W., Weerden, T., Widiawati, Y., Bannink, A., Beauchemin, K., Clark, H., Leytem, A., Kebreab, E., Ngwabie, N., and Vellinga, T.: Emissions from livestock and manure management, in: 2019 Refinement to the 2006 IPCC Guidelines for National Greenhouse Gas Inventories, IPCC, 2019.



- Giardino, C., Bresciani, M., Braga, F., Fabbretto, A., Ghirardi, N., Pepe, M., Gianinetto, M., Colombo, R., Cogliati, S., Ghebrehiwot, S.,
Laanen, M., Peters, S., Schroeder, T., Concha, J. A., and Brando, V. E.: First evaluation of prisma level 1 data for water applications,
840 *Sensors (Switzerland)*, 20, 1–16, <https://doi.org/10.3390/s20164553>, 2020.
- Gilks, W. R. and Berzuini, C.: Following a Moving Target—Monte Carlo Inference for Dynamic Bayesian Models, *Journal of the Royal
Statistical Society Series B: Statistical Methodology*, 63, 127–146, <https://doi.org/10.1111/1467-9868.00280>, 2001.
- Golston, L. M., Aubut, N. F., Frish, M. B., Yang, S., Talbot, R. W., Gretencord, C., McSpiritt, J., and Zondlo, M. A.: Natural Gas
Fugitive Leak Detection Using an Unmanned Aerial Vehicle: Localization and Quantification of Emission Rate, *Atmosphere*, 9, 333,
845 <https://doi.org/10.3390/atmos9090333>, 2018.
- Goopy, J., Onyango, A., Dickhoefer, U., and Butterbach-Bahl, K.: A new approach for improving emission factors for enteric methane
emissions of cattle in smallholder systems of East Africa – Results for Nyando, Western Kenya, *Agricultural Systems*, 161, 72–80,
<https://doi.org/10.1016/j.agsy.2017.12.004>, 2018.
- Goopy, J. P., Korir, D., Pelster, D., Ali, A. I. M., Wassie, S. E., Schlecht, E., Dickhoefer, U., Merbold, L., and Butterbach-Bahl, K.: Severe
850 below-maintenance feed intake increases methane yield from enteric fermentation in cattle, *British Journal of Nutrition*, 123, 1239–1246,
<https://doi.org/10.1017/S0007114519003350>, 2020.
- Gordon, N., Salmond, D., and Smith, A.: Novel approach to nonlinear/non-Gaussian Bayesian state estimation, *IEE Proceedings. Part F
(Radar and Signal Processing)*, 140, 107–113, <https://doi.org/10.1049/ip-f-2.1993.0015>, 1993.
- Gurmu, E., Ndung'u, P., Wilkes, A., Getahun, D., Graham, M., Leitner, S., Marquardt, S., Mulat, D., Merbold, L., Worku, T., Kagai, J., and
855 Arndt, C.: Comparison of Tier 1 and 2 methodologies for estimating intake and enteric methane emission factors from smallholder cattle
systems in Africa: a case study from Ethiopia, *Animal - Open Space*, 3, 100 064, <https://doi.org/10.1016/j.anopes.2024.100064>, 2024.
- Gålfalk, M., Nilsson Pålédal, S., and Bastviken, D.: Sensitive Drone Mapping of Methane Emissions without the Need for Supplemen-
tary Ground-Based Measurements, *ACS Earth and Space Chemistry*, 5, 2668–2676, <https://doi.org/10.1021/acsearthspacechem.1c00106>,
2021.
- 860 Hanna, S., Briggs, G. A., Hosker, R. P., and Smith, J. S.: Handbook on atmospheric diffusion, Department of Energy, [https://api.
semanticscholar.org/CorpusID:128993711](https://api.semanticscholar.org/CorpusID:128993711), 1982.
- Hegarty, R.: Applicability of short-term emission measurements for on-farm quantification of enteric methane, *Animal*, 7, 401–408,
<https://doi.org/10.1017/S1751731113000839>, 2013.
- Hutchinson, M., Oh, H., and Chen, W.-H.: A review of source term estimation methods for atmospheric dispersion events using static or
865 mobile sensors, *Information Fusion*, <https://doi.org/10.1016/j.inffus.2016.11.010>, 2017.
- Hutchinson, M., Liu, C., and Chen, W.: Source term estimation of a hazardous airborne release using an unmanned aerial vehicle, *Journal of
Field Robotics*, 36, 797–817, <https://doi.org/10.1002/rob.21844>, 2019.
- Hutchinson, M., Liu, C., Thomas, P., and Chen, W.-H.: Unmanned Aerial Vehicle-Based Hazardous Materials Response:
Information-Theoretic Hazardous Source Search and Reconstruction, *IEEE Robotics & Automation Magazine*, 27, 108–119,
870 <https://doi.org/10.1109/MRA.2019.2943006>, 2020.
- Jacob, D. J., Varon, D. J., Cusworth, D. H., Dennison, P. E., Frankenberg, C., Gautam, R., Guanter, L., Kelley, J., McKeever, J., Ott,
L. E., Poulter, B., Qu, Z., Thorpe, A. K., Worden, J. R., and Duren, R. M.: Quantifying methane emissions from the global scale
down to point sources using satellite observations of atmospheric methane, *Atmospheric Chemistry and Physics*, 22, 9617–9646,
<https://doi.org/10.5194/acp-22-9617-2022>, 2022.
- 875 Jaynes, E.: Probability theory : the logic of science, Cambridge University Press, Cambridge, ISBN 0521592712, 2003.



- Korir, D., Eckard, R., Goopy, J., Arndt, C., Merbold, L., and Marquardt, S.: Effects of replacing *Brachiaria* hay with either *Desmodium intortum* or dairy concentrate on animal performance and enteric methane emissions of low-yielding dairy cows, *Frontiers in Animal Science*, 3, 963 323, <https://doi.org/10.3389/fanim.2022.963323>, 2022a.
- 880 Korir, D., Marquardt, S., Eckard, R., Sanchez, A., Dickhoefer, U., Merbold, L., Butterbach-Bahl, K., Jones, C., Robertson-Dean, M., and Goopy, J.: Weight gain and enteric methane production of cattle fed on tropical grasses, *Animal Production Science*, 63, 120–132, <https://doi.org/10.1071/AN21327>, 2022b.
- Lan, X., Thoning, K., and Dlugokencky, E.: Trends in globally-averaged CH₄, N₂O, and SF₆ determined from NOAA Global Monitoring Laboratory measurements, <https://doi.org/https://doi.org/10.15138/P8XG-AA10>, 2024.
- Loisy, A. and Eloy, C.: Searching for a source without gradients: how good is infotaxis and how to beat it, *Proceedings of the Royal Society A: Mathematical, Physical and Engineering Sciences*, 478, 20220 118, <https://doi.org/10.1098/rspa.2022.0118>, 2022.
- 885 Loizzo, R., Guarini, R., Longo, F., Scopa, T., Formaro, R., Facchinetti, C., and Varacalli, G.: PRISMA: The Italian hyperspectral mission, in: *IGARSS 2018-2018 IEEE international geoscience and remote sensing symposium*, pp. 175–178, 2018.
- Moorhead, J. G.: *THE NEAR INFRARED ABSORPTION SPECTRUM OF METHANE*, 1932.
- Morales, R., Ravelid, J., Vinkovic, K., Korbeñ, P., Tuzson, B., Emmenegger, L., Chen, H., Schmidt, M., Humbel, S., and Brunner, D.:
890 Controlled-release experiment to investigate uncertainties in UAV-based emission quantification for methane point sources, *Atmospheric Measurement Techniques*, 15, 2177–2198, <https://doi.org/10.5194/amt-15-2177-2022>, 2022.
- Mwangi, P. M., Eckard, R., Gluecks, I., Merbold, L., Mulat, D. G., Gakige, J., Pinares-Patino, C. S., and Marquardt, S.: Impact of *Haemonchus contortus* infection on feed intake, digestion, liveweight gain, and enteric methane emission from Red Maasai and Dorper sheep, *Frontiers in Animal Science*, 4, 1212 194, <https://doi.org/10.3389/fanim.2023.1212194>, 2023.
- 895 Nathan, B. J., Golston, L. M., O'Brien, A. S., Ross, K., Harrison, W. A., Tao, L., Lary, D. J., Johnson, D. R., Covington, A. N., Clark, N. N., and Zondlo, M. A.: Near-Field Characterization of Methane Emission Variability from a Compressor Station Using a Model Aircraft, *Environmental Science & Technology*, 49, 7896–7903, <https://doi.org/10.1021/acs.est.5b00705>, 2015.
- Ndung'u, P. W., Bebe, B. O., Ondiek, J. O., Butterbach-Bahl, K., Merbold, L., and Goopy, J. P.: Improved region-specific emission factors for enteric methane emissions from cattle in smallholder mixed crop: livestock systems of Nandi County, Kenya, *Animal Production Science*,
900 59, 1136, <https://doi.org/10.1071/AN17809>, 2019.
- Nielsen, M. O., Kiani, A., Tejada, E., Chwalibog, A., and Alstrup, L.: Energy metabolism and methane production in llamas, sheep and goats fed high- and low-quality grass-based diets, *Archives of Animal Nutrition*, 68, 171–185, <https://doi.org/10.1080/1745039X.2014.912039>, 2014.
- Pandey, S., Gautam, R., Houweling, S., Van Der Gon, H. D., Sadavarte, P., Borsdorff, T., Hasekamp, O., Landgraf, J., Tol, P.,
905 Van Kempen, T., Hoogeveen, R., Van Hees, R., Hamburg, S. P., Maasackers, J. D., and Aben, I.: Satellite observations reveal extreme methane leakage from a natural gas well blowout, *Proceedings of the National Academy of Sciences*, 116, 26 376–26 381, <https://doi.org/10.1073/pnas.1908712116>, 2019.
- Park, M., An, S., Seo, J., and Oh, H.: Autonomous Source Search for UAVs Using Gaussian Mixture Model-Based Infotaxis: Algorithm and Flight Experiments, *IEEE Transactions on Aerospace and Electronic Systems*, 57, 4238–4254,
910 <https://doi.org/10.1109/TAES.2021.3098132>, 2021.
- Pasquill, F.: *The Estimation of the Dispersion of Windborne Material*, *Meteorological Magazine*, 1961.
- Paustian, K., Ravindranath, N., and van Amstel, A.: 2006 IPCC Guidelines for National Greenhouse Gas Inventories, no. Part 2 in Volume 4: Agriculture, Forestry and Other Land Use, [s.n.], 2006.



- 915 Pei, Z., Han, G., Mao, H., Chen, C., Shi, T., Yang, K., Ma, X., and Gong, W.: Improving quantification of methane point source emissions from imaging spectroscopy, *Remote Sensing of Environment*, 295, 113 652, <https://doi.org/https://doi.org/10.1016/j.rse.2023.113652>, 2023.
- Pinares-Patiño, C. S., Ulyatt, M. J., Waghorn, G. C., Lassey, K. R., Barry, T. N., Holmes, C. W., and Johnson, D. E.: Methane emission by alpaca and sheep fed on lucerne hay or grazed on pastures of perennial ryegrass/white clover or birdsfoot trefoil, *The Journal of Agricultural Science*, 140, 215–226, <https://doi.org/10.1017/S002185960300306X>, 2003.
- 920 Pirk, N., Aalstad, K., Westermann, S., Vatne, A., van Hove, A., Tallaksen, L. M., Cassiani, M., and Katul, G.: Inferring surface energy fluxes using drone data assimilation in large eddy simulations, *Atmospheric Measurement Techniques*, <https://doi.org/10.5194/amt-15-7293-2022>, 2022.
- Prather, M. J., Holmes, C. D., and Hsu, J.: Reactive greenhouse gas scenarios: Systematic exploration of uncertainties and the role of atmospheric chemistry, *Geophysical Research Letters*, 39, <https://doi.org/10.1029/2012gl051440>, publisher: American Geophysical Union (AGU), 2012.
- 925 Rao, K. S.: Uncertainty Analysis in Atmospheric Dispersion Modeling, *Pure and Applied Geophysics*, 162, 1893–1917, <https://doi.org/10.1007/s00024-005-2697-4>, 2005.
- Roger, J., Guanter, L., Gorroño, J., and Irakulis-Loitxate, I.: Exploiting the entire near-infrared spectral range to improve the detection of methane plumes with high-resolution imaging spectrometers, *Atmospheric Measurement Techniques*, 17, 1333–1346, <https://doi.org/10.5194/amt-17-1333-2024>, 2024a.
- 930 Roger, J., Irakulis-Loitxate, I., Valverde, A., Gorroño, J., Chabrilat, S., Brell, M., and Guanter, L.: High-Resolution Methane Mapping With the EnMAP Satellite Imaging Spectroscopy Mission, *IEEE Transactions on Geoscience and Remote Sensing*, 62, 1–12, <https://doi.org/10.1109/TGRS.2024.3352403>, 2024b.
- Sanz-Alonso, D.: Inverse problems and data assimilation, vol. 107 of *London Mathematical Society student texts* ;, Cambridge University Press, Cambridge, 1st ed. edn., ISBN 1-009-41433-X, 2023.
- 935 Saunio, M., Stavert, A. R., Poulter, B., Bousquet, P., Canadell, J. G., Jackson, R. B., Raymond, P. A., Dlugokencky, E. J., Houweling, S., Patra, P. K., Ciais, P., Arora, V. K., Bastviken, D., Bergamaschi, P., Blake, D. R., Brailsford, G., Bruhwiler, L., Carlson, K. M., Carrol, M., Castaldi, S., Chandra, N., Crevoisier, C., Crill, P. M., Covey, K., Curry, C. L., Etiopie, G., Frankenberg, C., Gedney, N., Hegglin, M. I., Höglund-Isaksson, L., Hugelius, G., Ishizawa, M., Ito, A., Janssens-Maenhout, G., Jensen, K. M., Joos, F., Kleinen, T., Krummel, P. B., Langenfelds, R. L., Laruelle, G. G., Liu, L., Machida, T., Maksyutov, S., McDonald, K. C., McNorton, J., Miller, P. A., Melton, J. R., Morino, I., Müller, J., Murguía-Flores, F., Naik, V., Niwa, Y., Noce, S., O’Doherty, S., Parker, R. J., Peng, C., Peng, S., Peters, G. P., Prigent, C., Prinn, R., Ramonet, M., Regnier, P., Riley, W. J., Rosentretter, J. A., Segers, A., Simpson, I. J., Shi, H., Smith, S. J., Steele, L. P., Thornton, B. F., Tian, H., Tohjima, Y., Tubiello, F. N., Tsuruta, A., Viovy, N., Voulgarakis, A., Weber, T. S., Van Weele, M., Van Der Werf, G. R., Weiss, R. F., Worthy, D., Wunch, D., Yin, Y., Yoshida, Y., Zhang, W., Zhang, Z., Zhao, Y., Zheng, B., Zhu, Q., Zhu, Q., and Zhuang, Q.: The Global Methane Budget 2000–2017, *Earth System Science Data*, 12, 1561–1623, <https://doi.org/10.5194/essd-12-1561-2020>, 945 2020.
- Scafutto, R. D. P. M., van der Werff, H., Bakker, W. H., van der Meer, F., and de Souza Filho, C. R.: An evaluation of airborne SWIR imaging spectrometers for CH₄ mapping: Implications of band positioning, spectral sampling and noise, *International Journal of Applied Earth Observation and Geoinformation*, 94, <https://doi.org/10.1016/j.jag.2020.102233>, 2021.
- 950 Shah, A., Allen, G., Pitt, J. R., Ricketts, H., Williams, P. I., Helmore, J., Finlayson, A., Robinson, R., Kabbabe, K., Hollingsworth, P., Rees-White, T. C., Beaven, R., Scheutz, C., and Bourn, M.: A Near-Field Gaussian Plume Inversion Flux Quantification Method, Applied to Unmanned Aerial Vehicle Sampling, *Atmosphere*, 10, 396, <https://doi.org/10.3390/atmos10070396>, 2019.



- Shah, A., Pitt, J. R., Ricketts, H., Leen, J. B., Williams, P. I., Kabbabe, K., Gallagher, M. W., and Allen, G.: Testing the near-field Gaussian plume inversion flux quantification technique using unmanned aerial vehicle sampling, *Atmospheric Measurement Techniques*, 13, 1467–1484, <https://doi.org/10.5194/amt-13-1467-2020>, 2020.
- 955 Sherwin, E., Rutherford, J., Chen, Y., Aminfard, S., Kort, E., Jackson, R., and Brandt, A.: Single-blind validation of spacebased point-source methane emissions detection and quantification, *Scientific Reports*, <https://doi.org/10.1038/s41598-023-30761-2>, 2023.
- Stull, R. B.: An introduction to boundary layer meteorology, Atmospheric sciences library, Kluwer Academic Publishers, Dordrecht, 2nd reprint. edn., ISBN 9027727686, 1989.
- Sutton, O.: The theoretical distribution of airborne pollution from factory chimneys, *Quarterly Journal of the Royal Meteorological Society*,
960 <https://doi.org/https://doi.org/10.1002/qj.49707331715>, 1947.
- Szopa, S., Naik, V., Adhikary, B., Artaxo, P., Bernsten, T., Collins, W., Fuzzi, S., Gallardo, L., Kiendler-Scharr, A., Klimont, Z., Liao, H., Unger, N., , and Zanis, P.: Short-Lived Climate Forcers, in: *Climate Change 2021: The Physical Science Basis. Contribution of Working Group I to the Sixth Assessment Report of the Intergovernmental Panel on Climate Change*, edited by Masson-Delmotte, V., Zhai, P., Pirani, A., Connors, S., Péan, C., Berger, S., Caud, N., Chen, Y., Goldfarb, L., Gomis, M., Huang, M., Leitzell, K., Lonnoy, E., Matthews,
965 J., Maycock, T., Waterfield, T., Yelekçi, O., Yu, R., , and Zhou, B., p. 817–922, Cambridge University Press, Cambridge, United Kingdom and New York, NY, USA, <https://doi.org/10.1017/9781009157896.008>, 2021.
- Särkkä, S. and Svensson, L.: *Bayesian Filtering and Smoothing*, Cambridge University Press, 2 edn., <https://doi.org/10.1017/9781108917407>, 2023.
- Thompson, R. L., Groot Zwaafink, C. D., Brunner, D., Tsuruta, A., Aalto, T., Raivonen, M., Crippa, M., Solazzo, E., Guizzardi, D., Regnier,
970 P., and Maisonnier, M.: Effects of extreme meteorological conditions in 2018 on European methane emissions estimated using atmospheric inversions, *Philosophical Transactions of the Royal Society A: Mathematical, Physical and Engineering Sciences*, 380, 20200443, <https://doi.org/10.1098/rsta.2020.0443>, 2022.
- van Hove, A., Aalstad, K., and Pirk, N.: Inferring methane emissions from African livestock by fusing drone, tower, and satellite data, <https://doi.org/10.5281/zenodo.14214699>, 2024a.
- 975 van Hove, A., Aalstad, K., and Pirk, N.: Guiding drones by information gain, in: *Proceedings of the 5th Northern Lights Deep Learning Conference (NLDL)*, edited by Lutchyn, T., Ramírez Rivera, A., and Ricaud, B., vol. 233 of *Proceedings of Machine Learning Research*, pp. 89–96, PMLR, <https://proceedings.mlr.press/v233/hove24a.html>, 2024b.
- Van Leeuwen, P. J.: Representation errors and retrievals in linear and nonlinear data assimilation, *Quarterly Journal of the Royal Meteorological Society*, 141, 1612–1623, <https://doi.org/10.1002/qj.2464>, 2015.
- 980 Varon, D. J., Jacob, D. J., McKeever, J., Jervis, D., Durak, B. O. A., Xia, Y., and Huang, Y.: Quantifying methane point sources from fine-scale satellite observations of atmospheric methane plumes, *Atmospheric Measurement Techniques*, 11, 5673–5686, <https://doi.org/10.5194/amt-11-5673-2018>, 2018.
- Vechi, N. T., Mellqvist, J., and Scheutz, C.: Quantification of methane emissions from cattle farms, using the tracer gas dispersion method, *Agriculture, Ecosystems & Environment*, 330, 107885, <https://doi.org/10.1016/j.agee.2022.107885>, 2022.
- 985 Vergassola, M., Villermaux, E., and Shraiman, B. I.: ‘Infotaxis’ as a strategy for searching without gradients, *Nature*, <https://doi.org/10.1038/nature05464>, 2007.
- Vergé, C., Dubarry, C., Del Moral, P., and Moulines, E.: On parallel implementation of sequential Monte Carlo methods: the island particle model, *Statistics and Computing*, 25, 243–260, <https://doi.org/10.1007/s11222-013-9429-x>, 2015.



- Villa, T., Gonzalez, F., Miljevic, B., Ristovski, Z., and Morawska, L.: An Overview of Small Unmanned Aerial Vehicles for Air Quality
990 Measurements: Present Applications and Future Prospectives, *Sensors*, 16, 1072, <https://doi.org/10.3390/s16071072>, 2016.
- Vinković, K., Andersen, T., De Vries, M., Kers, B., Van Heuven, S., Peters, W., Hensen, A., Van Den Bulk, P., and Chen, H.: Evaluating the
use of an Unmanned Aerial Vehicle (UAV)-based active AirCore system to quantify methane emissions from dairy cows, *Science of The
Total Environment*, 831, 154 898, <https://doi.org/10.1016/j.scitotenv.2022.154898>, 2022.
- Western, L. M., Ramsden, A. E., Ganesan, A. L., Boesch, H., Parker, R. J., Scarpelli, T. R., Tunnicliffe, R. L., and Rigby, M.: Estimates
995 of North African Methane Emissions from 2010 to 2017 Using GOSAT Observations, *Environmental Science & Technology Letters*, 8,
626–632, <https://doi.org/10.1021/acs.estlett.1c00327>, 2021.
- Wolz, K., Leitner, S., Merbold, L., Wolf, B., and Mauder, M.: Enteric methane emission estimates for Kenyan cattle in a night-
time enclosure using a backward Lagrangian Stochastic dispersion technique, *Theoretical and Applied Climatology*, 147, 1091–1103,
<https://doi.org/10.1007/s00704-021-03868-7>, 2022.
- 1000 Wratt, D. S., Gimson, N. R., Brailsford, G. W., Lassey, K. R., Bromley, A. M., and Bell, M. J.: Estimating regional methane emissions from
agriculture using aircraft measurements of concentration profiles, *Atmospheric Environment*, 2001.
- Xiao, C., Fu, B., Shui, H., Guo, Z., and Zhu, J.: Detecting the sources of methane emission from oil shale mining and processing using
airborne hyperspectral data, *Remote Sensing*, 12, <https://doi.org/10.3390/rs12030537>, 2020.
- Yang, S., Talbot, R. W., Frish, M. B., Golston, L. M., Aubut, N. F., Zondlo, M. A., Gretencord, C., and McSpirtt, J.: Natural Gas Fugitive
1005 Leak Detection Using an Unmanned Aerial Vehicle: Measurement System Description and Mass Balance Approach, *Atmosphere*, 9, 383,
<https://doi.org/10.3390/atmos9100383>, 2018.



Table B1. Overview of methane emission rate estimates obtained by the mass balance method, the Bayesian inference method, and the IPCC Tier 2 workflow with $\pm 20\%$ uncertainty range (Paustian et al., 2006). The cases are defined as: (a) using concentration observations, (b) using concentration observations and mean wind speed data from the drone, (c) using concentration observations and mean wind speed, mean wind direction and diffusivity data derived from Monin Obukhov Similarity Theory. Emission rate estimates are given in q [$\text{g hd}^{-1} \text{h}^{-1}$], where hd is short for head, except for the last column which presents estimates in Q [g h^{-1}], i.e. for the entire herd. One standard deviation uncertainty is reported. Dates of drone flights are denoted by [DD/MM]; AM and PM indicate drone flights conducted in the morning before feeding and in the afternoon after feeding, respectively. Wind speed (V_{EC} [m s^{-1}]) and wind direction (ϕ_{EC} [$^\circ$]) data are from the flux tower during the mass balance flight. Further notation: (♦) Unreliable drone flight results due to unfavorable wind conditions (following Yang et al. (2018)); (♠) Unreliable estimates due to a low signal-to-noise ratio caused by a weak emission source; (•) Estimates using a narrower prior for wind direction: $\mathcal{U}(30, 135)$; (★) IPCC Tier 1 value with $\pm 50\%$ uncertainty range (Paustian et al., 2006).

Date	Herd		Wind		Mass balance		Bayesian inference			IPCC Tier 2 value	
	Animals	Count	V_{EC}	ϕ_{EC}	q	q , case a	q , case b	q , case c	q	Q	
[DD/MM]	[-]	[-]	[m s^{-1}]	[$^\circ$]	[$\text{g hd}^{-1} \text{h}^{-1}$]	[$\text{g hd}^{-1} \text{h}^{-1}$]	[$\text{g hd}^{-1} \text{h}^{-1}$]	[$\text{g hd}^{-1} \text{h}^{-1}$]	[$\text{g hd}^{-1} \text{h}^{-1}$]	[g h^{-1}]	
02/03 AM	cows	101	3.5 ± 0.9	27 ± 24	18.3 ± 2.5	18.7 ± 4.7	11.9 ± 1.7	13.0 ± 1.4	10.0 ± 2.0	$1,005 \pm 201$	
02/03 PM	cows	101	5.2 ± 1.5	56 ± 16	10.6 ± 3.1	15.1 ± 2.8	13.0 ± 1.5	17.4 ± 1.5	10.0 ± 2.0	$1,005 \pm 201$	
02/03 AM	heifers	208	3.7 ± 0.8	61 ± 21	5.2 ± 1.3	6.5 ± 1.7	4.4 ± 0.8	4.5 ± 0.6	6.9 ± 1.4	$1,438 \pm 288$	
02/03 PM	heifers	208	5.7 ± 1.3	66 ± 11	5.9 ± 1.4	13.3 ± 3.0	12.0 ± 2.0	13.5 ± 1.3	6.9 ± 1.4	$1,438 \pm 288$	
06/03 AM	heifers	206	3.9 ± 0.9	48 ± 13	5.1 ± 1.3	4.6 ± 1.3	3.1 ± 0.9	4.0 ± 0.5	6.9 ± 1.4	$1,425 \pm 285$	
06/03 PM	heifers	206	5.8 ± 1.5	70 ± 14	8.2 ± 1.7	7.2 ± 1.4	5.4 ± 0.8	7.4 ± 0.7	6.9 ± 1.4	$1,425 \pm 285$	
05/03 AM	steers	127	4.9 ± 1.1	61 ± 12	9.5 ± 2.1	6.1 ± 1.6	4.0 ± 0.8	5.7 ± 0.9	5.6 ± 1.1	710 ± 142	
05/03 PM	steers	127	6.7 ± 1.6	53 ± 13	7.4 ± 2.5	8.1 ± 2.3	7.5 ± 1.3	8.5 ± 1.1	5.6 ± 1.1	710 ± 142	
03/03 AM	slick herd	148	2.0 ± 0.9	354 ± 59	3.3 ± 2.2 ♦	11.4 ± 3.8	6.9 ± 2.4	7.0 ± 1.1	10.4 ± 2.1	$1,539 \pm 308$	
03/03 PM	slick herd	148	4.9 ± 1.4	55 ± 23	12.5 ± 2.1	12.5 ± 3.6	7.5 ± 1.2	11.9 ± 1.1	10.4 ± 2.1	$1,539 \pm 308$	
04/03 AM	camels	42	1.7 ± 0.7	289 ± 47	-2.6 ± 7.4 ♦	3.4 ± 2.3	2.8 ± 1.7	2.3 ± 1.2	5.3 ± 2.6 ★	231 ± 116 ★	
04/03 PM	camels	42	4.3 ± 1.4	58 ± 28	8.4 ± 6.9	12.9 ± 4.5	8.8 ± 2.8	11.0 ± 2.3	5.3 ± 2.6 ★	231 ± 116 ★	
07/03 AM	lactating ewes	173	3.1 ± 1.3	83 ± 26	0.2 ± 0.7 ♠	0.9 ± 0.4	0.8 ± 0.3	0.9 ± 0.3	0.6 ± 0.1	112 ± 22	
07/03 PM	lactating ewes	173	4.3 ± 1.4	90 ± 26	4.2 ± 1.4 ♠	0.8 ± 0.4	0.7 ± 0.3	0.8 ± 0.3	0.6 ± 0.1	112 ± 22	
01/03 AM	dry does	197	2.4 ± 0.7	60 ± 35	4.8 ± 1.3 ♦♠	0.8 ± 0.5 ♦	0.7 ± 0.4 ♦	0.5 ± 0.3	0.7 ± 0.1	141 ± 28	
01/03 PM	dry does	197	4.6 ± 1.3	46 ± 21	3.9 ± 1.5 ♠	1.7 ± 0.7 ♦	1.5 ± 0.6 ♦	1.8 ± 0.5	0.7 ± 0.1	141 ± 28	
29/02 PM	pregnant does	124	5.6 ± 1.3	51 ± 17	0.8 ± 2.7 ♠	1.3 ± 0.8 ♦	1.1 ± 0.6 ♦	1.3 ± 0.7	0.6 ± 0.1	74 ± 15	
07/03 AM	pregnant does	124	1.4 ± 0.6	12 ± 67	1.7 ± 1.5 ♦♠	0.8 ± 0.6	0.6 ± 0.4	0.7 ± 0.3	0.6 ± 0.1	74 ± 15	
07/03 PM	pregnant does	124	4.2 ± 1.3	62 ± 28	4.2 ± 1.9 ♠	1.2 ± 1.2	1.2 ± 1.0	1.0 ± 0.5	0.6 ± 0.1	74 ± 15	
01/03 AM	weaner kids	118	3.6 ± 1.1	58 ± 15	5.0 ± 1.9 ♠	0.8 ± 0.6 ♦	0.6 ± 0.4 ♦	0.7 ± 0.5	0.7 ± 0.1	79 ± 16	
01/03 PM	weaner kids	118	6.2 ± 1.4	49 ± 12	11.1 ± 2.3 ♠	0.8 ± 0.6 ♦	0.8 ± 0.6 ♦	0.9 ± 0.6	0.7 ± 0.1	79 ± 16	